Increased strength in carbon-poly(ether ether ketone) composites from material extrusion with rapid microwave post processing

Jia-Ruey Ai,[1] Siyuan Li,[2] Bryan D. Vogt[1,*]

[1]Department of Chemical Engineering, The Pennsylvania State University, University Park, PA 16802

[2]Department of Polymer Engineering, University of Akron, Akron, OH 44325

*To whom correspondence should be addressed: bdv5051@psu.edu (B.D.V.)

ABSTRACT:

One critical challenge for commercial products via material extrusion 3D printing is their inferior the mechanical properties in comparison to injection molding; in particular, 3D printing leads to weaker properties perpendicular to the plane of the printed roads (z-direction). Here, rapid (≤20 s) post-processing of 3D printed carbon- poly(ether ether ketone) (PEEK) with microwaves is demonstrated to dramatically increase the modulus, such that the *z*-direction after microwave processing (2.7-3.8 GPa) exhibits a higher elastic modulus than the maximum in any direction for the as-printed part (2.3 GPa). Additionally, the stress at break in the *z*-orientation is increased by an order of magnitude by microwaves to be consistent with other print orientations in the as-printed state. The rapid heating and cooling by coupling of the microwave energy with the carbon filler in the PEEK does not increase the crystallinity of the PEEK, so the increased mechanical properties are attributed to improved interfaces between printed roads. This simple microwave post-processing enables large increases in the elastic modulus of the printed parts and can be tuned by the microwave power. As PEEK is generally difficult to print, these concepts can likely be applied to other commercial engineering plastic filaments that contain carbon or other fillers that are microwave active to rapidly post process 3D printed thermoplastics and does not require the modification of filament with selective placement of the carbon. Additionally, these results demonstrate that the average crystallinity does not necessarily correlate with the strength of 3D printed semicrystalline plastics due to the importance of the details of the interface between adjacent printed roads.

KEYWORDS: Engineering Plastics; Material Extrusion; FDM; Fused Filament Fabrication

1. INTRODUCTION

Additive manufacturing of high-performance engineering plastics by material extrusion (MatEx) has rapidly advanced in recent years [1, 2]. The mechanical performance of these printed thermoplastic parts tends to suffer from a number of drawbacks in comparison to traditionally processed plastics [3, 4], including lower elastic modulus, anisotropic properties and decreased toughness/ductility. Significant efforts have been undertaken to optimize the print tools and process conditions to minimize these adverse effects in MatEx 3D printing based on fused filament fabrication (FFF) [5-7]. Many of the challenges can be attributed to the strength of the weld between adjacent printed roads and thus there have been many efforts to develop routes to measure and predict the interfacial strength [8-11]. The characteristics of the polymer flow (rheology) during the print [12] determine the interface development [11], entanglements [13], and melt elasticity/chain alignment that could produce deformation or residual stresses in the printed part [14]. One simple route to address the residual stresses in the parts is through thermal post to allow the stresses to relax [15].

For MatEx, glassy thermoplastics are commonly employed, such as polylactic acid (PLA) [16], acrylonitrile-butadiene-styrene (ABS) [17] and polyetherimide (PEI) [18], where the glass transition temperature (T_g) is a critical characteristic associated with printing [14]. The non-Arrhenius approach to T_g leads to a marked slowdown in the polymer dynamics on cooling as T_g is approached [19], which leads to locked-in non-equilibrium chain conformation and added residual stress in the printed part [14]. The performance of these (predominately) amorphous plastics is typically limited by the mechanical properties that can be attributed to the weld lines between printed roads [9], where insufficient interdiffusion occurs [20]. To address these challenges with the mechanical performance of 3D printed glassy polymers, a variety of approaches have been proposed. The viscosity of the polymer at temperatures near T_g is high, so heating near T_g can relax segmental stresses and improve the inter-road welds without significant deformation of the macroscopic structure of the 3D printed object [21]. Alternatively, the density of the printed plastic can be enhanced to improve mechanical properties through cold isostatic pressing, while completely arresting flow [22]. Green and coworkers recognized that the primary loci for failure was the interface between printed roads and thus localization of heating at this interface via inclusion of carbon nanotubes at the surface of the filaments to couple microwave energy for annealing can dramatically increase the mechanical performance without loss of the dimensional accuracy [23]. This microwave process illustrated a 275% increase in the weld fracture strength of PLA, but requires re-engineering of the filaments with a carbon nanotube coating [23] and/or modification of the printer to enable the inductive heating during the print [24-27]. This large improvement in mechanical performance suggests that rapid processing with inductive heating could provide significant enhancements that are not possible with tradition approaches. However, microwave post processing of carbon-PLA composites led to only marginal (<20%) increases in tensile strength [28]. There is evidence that nanoparticles on the surface of filaments can on their own act to improve the adhesion between printed roads [29], so this might be one reason for the difference in mechanical performance between carbon nanotube coatings and uniform carbon fiber composites but this has not been adequately investigated.

Despite the biased preference of glassy plastics for 3D printing, semicrystalline plastics offer the potential for improved mechanical performance due to differences in the solidification and requirements for a strong interface [30]. The dynamics associated with semicrystalline polymers differs tremendously from glassy polymers as there is a step-change in viscosity on crystallization, such that the mobility of the polymer is effectively halted on crystallization. This enhanced mobility near the solidification temperature can provide printed parts with mechanical properties that can be adequate for a variety of applications, but the stresses developed on crystallization can generally act to deform the printed object [31-33]. There have been a variety of approaches taken to minimize the deformation of the printed structure on crystallization of the filament, which include use of a large brim [33], inclusion of additives to minimize crystallization [34], and dilution of the crystalline material with a filler [35]. There is potential for significant improvements in mechanical properties of semicrystalline polymers on post processing to generate better defined crystals across the interfaces between printed roads. The temperature dependence of the viscosity of semicrystalline polymers tends to limit the post-processing as melting the crystals will tend to produce significant flow. The topology of the chains tends to be locked in place on annealing at temperatures below T_m, as the crystals effectively act as physical crosslinks. Under these conditions, only local motions are allowable to produce some secondary crystallization by the amorphous segments in the polymer, but this limits significant rearrangement of the polymer conformation to dramatically enhance mechanical performance of semicrystalline engineering plastics as motion across the interface is likely necessary due to the alignment of the chains in the print direction [36]. One alternative to temperature is to use non-solvent vapors to provide mobility to the polymer to improve the mechanical properties of 3D printed semicrystalline polymers [37].

In this work, we demonstrate the potential of microwave energy to rapidly heat and cool a 3D printed structure using a commercially available carbon-PEEK composite filament (containing 10 wt% carbon fiber) to enhance the mechanical properties of the part. This methodology builds upon the pioneering work of Green and coworkers, who used carbon nanotube coating on PLA filaments to provide localized heating to the interfaces between printed roads [23]. Although the size of the printed specimen is limited by the microwave size, there are a variety of industries that have already adopted microwaves for processing that produce large area objects, notably in aerospace for curing of carbon fiber thermosets [38], vulcanization of rubber, and powder drying for mineral processing [39]. These large industrial microwaves, including those developed for roll-to-roll processing [40], should provide the scale to enable microwave post-processing of most 3D printed parts based on the build size limits of most production MatEx printers and scale-up challenges for industrial microwaves have mostly been overcome [41]. In the work presented here, the carbon is dispersed throughout the filament, so heating will not only be centered at the interface. In prior studies, the coating of the filament localizes the heating but here the heating will occur everywhere in the printed part. However, the microwaves eliminate the initial constraints of heat transfer when compared with oven annealing and improve the time resolution for short high temperature annealing, which can allow for more efficient processing [38]. Moreover in comparison to early work with microwave processing for AM, this approach is more readily transferable due to the prevalence of commercial carbon-filled composite filaments on the market [42]. The tensile properties of the printed carbon PEEK were examined as a function of print orientation and post processing at low (100 W, 20 s) and high (200 W, 10 s) microwave power. This microwave processing rapidly heated the printed specimen to locally melt the PEEK crystals, but also allows for rapid cooling on cessation of the application of radiation. Rapid cooling tends to impede the crystallization of the PEEK and the crystallinity of the PEEK decreases with the microwave post processing. However, the short heating time minimizes deformation of printed object. The microwave processing tends to increase the elastic modulus by a factor of 2-3 for all print directions. Despite the preservation of some anisotropy in the mechanical properties associated with print direction, the end-on (YZ direction) printed specimen exhibits a higher elastic modulus after microwave processing than the as-printed specimens printed flat (XY) or edge-on (XZ). These results demonstrate the potential to rapidly improve the mechanical performance of 3D printed composites with microwaves, which may be applicable to other carbon-filled composites filaments that are commercially available and utilize high performance engineering polymer matrices.

2. MATERIAL AND METHODS

2.1. Materials and Characterization: Carbon PEEK filament was acquired from Roboze, Inc. The PEEK contained 10 wt% short carbon fiber loading per data sheet specifications. To remove adsorbed water, the filament was dried at 100˚C for 12 h using the HT dryer associated with the Roboze One +400 Xtreme printer. The dried filaments were used for printing without removal from the chamber, while small pieces of the dried filament were removed for thermal analysis. The thermal properties of the carbon PEEK were assessed by differential scanning calorimetry (DSC, TA Instruments Q200). The DSC experiments were performed at 10°C min^{-1} in hermetically sealed aluminum pans (DSC Consumables, Inc.) under a nitrogen atmosphere. The thermograms from DSC were recorded on heating from 40° to 400 °C. In all cases, 4-6mg of polymer composite were used with samples examined from the filament, after printing and after post processing. The first heating was used to calculate the crystallinity of the specimens from the integrated enthalpy associated with the endotherm on melting. The enthalpy was normalized by the mass of PEEK in the specimen based on 10 wt% carbon fiber in the composite. The fractional crystallization was determined as: $\%Crystallinity = \frac{\Delta H_{exp}}{\Delta H^{\circ}}$, where ΔH_{exp} is the experimentally measured enthalpy of crystallization and ΔH° is the reported enthalpy of crystallization for PEEK (122.5 J g^{-1}) [43]. X-ray diffraction (XRD, Bruker AXS D8 Discover) with copper K_α radiation (λ = 1.54 Å) at 40 kV and 35 mA was used to determine the crystalline phase of the PEEK. The diffraction was measured from 10° to 35° with a step size of 0.01° in θ -2θ mode using a standard 10 mm slit.

2.2. 3D Printing: The carbon PEEK filaments were printed into standard tensile (ASTM D638 type V) specimens using a Roboze One +400 Xtreme 3D printer that is designed for printing high performance engineering plastics and was equipped with a 0.4 mm E3D hardened steel nozzle. This hardened nozzle decreases the abrasion losses from the carbon fibers in the filament. The extrusion temperature (430°C) and printing speed (20 mm/s) were selected to match the original calibration builds for the Roboze printer. The composite was printed onto a polyetherimide (PEI) sheet held via a vacuum system with the building platform temperature set to 130 °C. All layer heights were set as 0.2 mm layer height with 1 layer of perimeter. The g-code was generated via Simplify3D (version 4.1.2). Tensile bars were printed with 100% infill and 0°/90° alternating print orientation. For statistics, 9 specimens were printed in parallel in the same build orientation at same time. The tensile bars were printed in flat (XY), edge-on (XZ) and stand-on (YZ) build orientations. Layers were printed with 0°/90° orientation.

2.3. Microwave Post-Processing: The printed tensile bars were subjected to controlled microwave radiation for inductive heating from the carbon fiber fill using a research microwave (BP-210, Microwave Research and Applications, Inc.) as shown in Figure S1 in the Appendix. The printed specimens were held on glass slides and placed into the center of a quartz tube that provides potential for flow chemistry through the microwave. In this case, the tube is used to purge the atmosphere surrounding the printed carbon PEEK with argon gas. To minimize the residual oxygen, the tube was purged at 100 mL/min for >10 min prior to heating with microwaves. The power of the microwave was systematically varied along with the exposure time to understand the post processing window. When the microwave power was 400 W or greater, decomposition of polymer was observed from FTIR measurements, even with only 5 s of microwave exposure. With lower microwave power conditions at 200 W for 20 s or 100 W for 40 s, decomposition of polymer was not observed but the specimens seriously deformed. Due to the geometry of the microwave chamber, it was not possible to measure the temperature of the specimens during microwave processing with an IR camera as commonly reported in the literature [44], Thus, we relied on observations about the changes in the macroscopic structure to select the microwave processing conditions that should impact the mechanical properties. In this case, the power was set to 200 W or 100 W with shorter microwave post-processing times to prevent decomposition of polymer and to limit the deformation of the test specimens. Images of the test specimens with significant deformation are shown in Figure S2 in the Appendix. It should be noted that the exact conditions necessary will be specific to the microwave and details of the cavity as determined through detailed microwave engineering [45]. For this reason, the samples were always carefully loaded to the same position in the microwave with the same ceramic boat supporting the printed specimens.

2.4. 3D Scanning: To quantify changes in the dimensional accuracy with microwave post processing, a blue light scanning camera (Polyga, HDI-C109) equipped with a rotatory stage was used to reconstruct the 3D structure within FlexScan3D software (Polyga, version 3.3.12). Prior scanning, the camera system was calibrated with calibrating checkerboard on the rotary stage and follow procedures provided from manufacturer. For improved contrast, specimens were sprayed with a thin layer of AESUB blue 3D scanning spray (AESUB). The specimen was then fixed to the rotary stage with nonhardening clay (Sargent Art). 12 images were captured each scan and total of 2 scans were performed for each sample to ensure the full structure was captured. The 3D structure was reconstructed within FlexScan3D using a mesh density of 100% and interval spacing of 0.06. The two scans were then aligned and combined into one 3D structure. The finalized 3D structures were then compared with original CAD file within the GOM inspect 2019 software with three-points alignment method to produce a false color map to illustrate the dimensional accuracy.

2.5. Mechanical Testing: The mechanical properties of the printed carbon PEEK specimens were determined in tensile mode using an MTS 50kN load frame (Criterion Model 43). The load frame was equipped with a 5 kN force sensor and a video extensometer. The video extensometer was used to provide an accurate measure of the deformation within the gauge region of the tensile dogbone specimens. The displacement rate was 10 $\text{mm}\cdot\text{min}^{-1}$ for all specimens. These test parameters are consistent with ASTM D638 for the tensile test of plastic materials.

2.6. Imaging: The failure surfaces of the tensile specimens were examined using scanning electron microscopy (SEM, Thermo Scientific Q250). The specimens were obtained after mechanical testing and the height of the sample was cut to accommodate the SEM chamber. The specimens were mounted on a sample puck with carbon conductive tape (Nisshin Em Co., Ltd.). No coating or other modifications were made to the fracture surface being imaged. The SEM measurements were performed in high vacuum mode to minimize oxidation. The measurements used an accelerating voltage of 3 kV and current of 53 pA. An EDT detector was used to capture secondary electrons. The images were acquired using the image integration function to improve resolution.

The internal structure of carbon PEEK printed specimen was elucidated with X-ray microcomputed tomography (μCT, Zeiss Versa 620). The μCT scanner operated at 80 kV/ 125 μA without a filter and X-ray images were recorded every 0.4° over a range of 180°. The electron density differences between the polymer matrix and carbon fiber provided contrast for μCT to directly visualize the carbon fibers within the polymer matrix. The carbon fiber orientation in the printed parts was determined using Avizo (software, version 2020.2, Thermo Fisher Scientific). The relative orientation of the fibers to the print direction was quantified using the Herman's orientation factor, *f*, by manually summing the orientations of all the carbon fibers in the field of view. The Herman's orientation factor is given as: $f = \frac{3\langle\cos^2\alpha\rangle - 1}{2}$, where α is the angle of an individual carbon fiber relative to the print direction.

Lower resolution μCT scans were used the GE v|tome|x L300 multiscale nano/μCT system operating at 50kV/200 μA without a filter. The X-ray images were recorded every 0.4° over 180°. These lower resolution scans enabled direct visualization of the internal voids and surface topology of the printed parts before and after post processing with microwaves. The size of the voids within the printed parts was quantified using the μCT reconstruction within the Avizo software.

3. RESULTS AND DISCUSSION

3.1 Additive manufactured polymer composite assisted with microwave post-processing. Figure 1a illustrates the three different build orientations (flat XY, edge-on XZ and stand-on YZ) that were investigated. For both XY and XZ orientation, the printed specimen includes roads that extend along the full specimen in the direction of the applied force, while the strength of the specimen printed in YZ orientation relies fully upon the strength of the printed road interfaces during the tensile test. The relatively fast cooling through the crystallization (T_c) and glass transition (T_g) temperatures of the PEEK during the print tends to lead to weak interfaces between the printed roads as there is limited interdiffusion of chains and chain orientation from flow limits crystallization between the printed roads [46]. Post-processing with microwaves is examined here as a route to improve the properties of the interfaces as schematically illustrated in Figure 2b. The carbon fibers are aligned by flow and adsorb the microwaves to promote local inductive heating that can act to quickly heat the composite, but also cooling is generally rapid on cessation of the microwave radiation [23, 47, 48]. The inductive heating overcomes limitations associated with heat transfer to rapidly heat the volume of the specimen to temperature, so there is no time delay in annealing the middle of the specimen as would be the case in an oven. As the result of both the uniform heating that can decrease the heat exposure time and the large ΔT due to the microwave not heating the environment around the specimen providing accelerated heat transfer especially near the surface of the printed specimen, the flow of the polymer can be limited to minimize large scale structural changes with the use of microwaves.

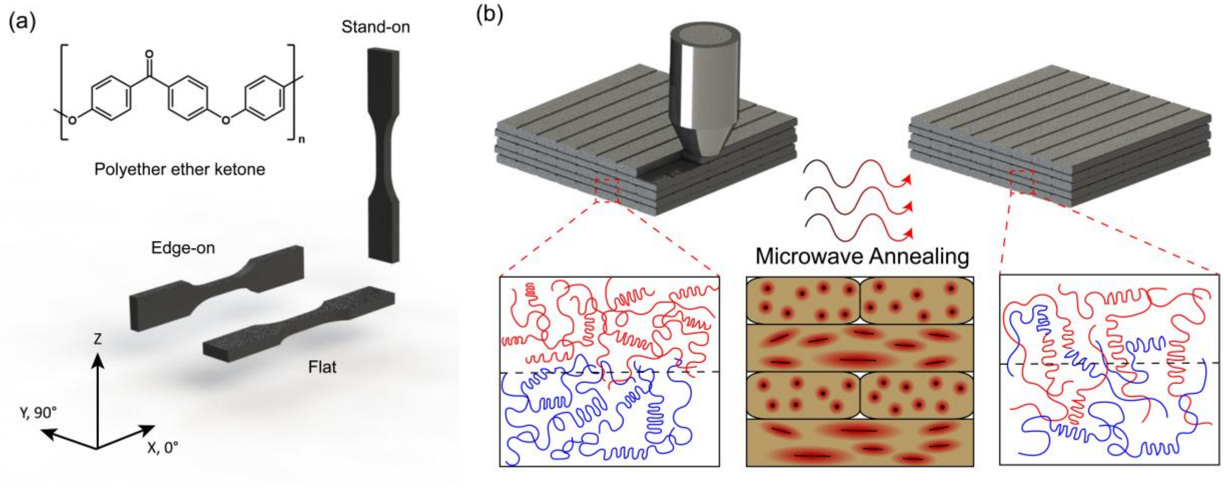

Figure 1. (a) Schematic showing printed carbon PEEK with different build orientations along with PEEK chemical structure. (b) Schematic illustrating the printed road directions and the proposed effect of microwave post-processing on the chain conformation at the interface between roads of additive manufactured carbon PEEK.

3.2 Impact of build orientation and post-processing on tensile properties. Figure 2 illustrates how the print orientation and microwave post-processing impacts the tensile stress-strain behavior of the 3D printed carbon PEEK (containing 10 wt% short carbon fiber). When examining the as-printed specimens, there is a significant reduction in the mechanical properties in terms of both the ultimate tensile stress and strain at break when printed in the stand-on build orientation. This significant anisotropy in mechanical properties is common for most polymers printed by MatEx [49, 50] with few exceptions [51, 52]. However, the improvement in the stress strain performance after the microwave processing is quite striking. As shown in Figure 2a for the composite printed in the flat build orientation, there is a factor of 3-4 increase in the ultimate stress after microwave processing and a commensurate increase in the slope of the stress-strain curve. These changes in the stress-strain behavior are indicative of significant enhancements in the strength of the printed parts. It should be noted that the waviness in the tensile curves in some case is a result of repositioning of the video extensiometer; the stress-strain curve based on crosshead displacement is smooth for all specimens examined. A similar change in the mechanical performance is observed with the edge-on build orientation (Figure 2b), but the enhancement appears in cases to be more significant in this orientation. For the stand-on build orientation (Figure 2c), the modulus clearly increases significantly with the use of microwave post-processing, but the specimens remain significantly more brittle than for the other build orientations with the strain at break being approximately ¼ that of the flat or edge-on build orientations. All of the individual stress-strain curves for the printed specimens are included in the appendices (Figures S3-S5) for completeness. These results illustrate that the microwave post processing can significantly increase the mechanical performance, but the extent of improvement appears to be dependent on the build orientation.

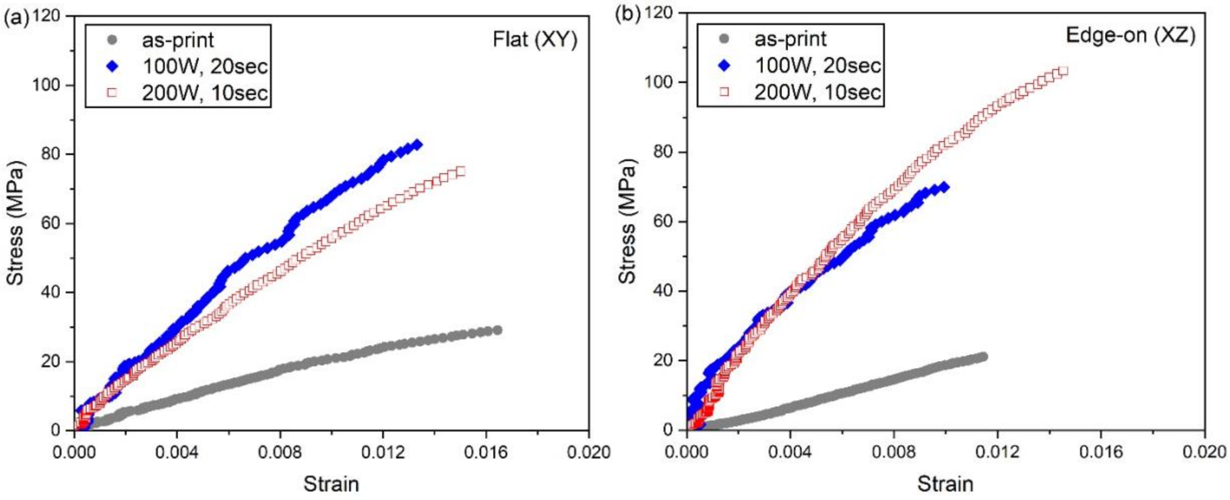

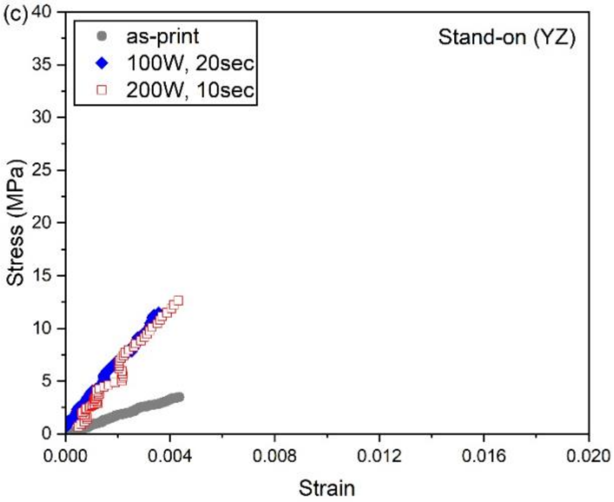

Figure 2. Representative stress-strain curves for (a) flat, (b) edge-on and (c) stand-on build orientations of carbon PEEK with (●) no post processing, (◆) 100 W for 20 s, and (□) 200 W for 10 s microwave irradiation.

To better quantify the effect of microwave post processing on the mechanical properties of the carbon PEEK composite, the average properties are reported in Figure 3 with the standard error shown as the error bars in the plots. The enhancement in elastic modulus by microwave post-processing is clear from Figure 3a with the modulus increasing from approximately 2 GPa to greater than 5.5 GPa. Although the average modulus with the lower power is greatest, the difference in modulus between the two microwave powers examined is not significant. The elastic moduli of the as-printed and post processed at 100 W specimens are only marginally impacted by the change from flat to edge-on build orientation, but there is a significant difference in modulus with 200 W microwave post-processing with a higher modulus using the edge-on build orientation. Similarly, the elastic modulus exhibits the largest improvement with the 200 W microwave post-processing when printed in the stand-on build orientation, but the absolute value of the elastic modulus is significantly smaller when compared with other build orientations after microwave post processing. However, the elastic modulus after microwave post processing in the stand-on build orientation is greater than the as-printed modulus in the flat or edge-on build orientation. The microwave post-processing only marginally impacts the strain at break for the carbon peak with all specimens failing at less than 2% strain (Figure 3b). Here, the carbon fibers within the composites impedes the rearrangement of the molecule orientations for the PEEK chains, so the composites are not as ductile as neat PEEK [53]. This composite driven brittleness of the composite leads to a limited effect of microwave processing on the strain at break for the printed parts in general. Figure 3c shows the toughness of printed sample, which is associated with the capacity of the part to absorb energy prior to failure. From the tensile data, this toughness is calculated as the area under the stress - strain curve. The inferior toughness for the stand-on build orientation can be mostly attributed to its much lower strain at break, irrespective of post processing. The microwave post processing promotes interfacial welding to increase the stress required for deformation to enhance its capability to absorb energy prior failure for the printed composites. This increased strength is captured by the ultimate tensile strength (UTS) shown in Figure 3d. The maximum stress prior to failure is increased with microwave post processing, but there is limited effect of the microwave conditions on the UTS for the 3D printed cPEEK. The differences in the anisotropy of Young's modulus and UTS for different build orientations are shown in Figure S6. Overall, flat and edge-on build orientations outperform stand-on build orientation regardless of microwave post processing, where the printed roads act similar to carbon fiber composites with fiber pull-out or fiber fracture being required before catastrophic failure [54]. As expected the mechanical performance of the 3D printed composites is less than reported values in the literature for continuous carbon fiber-PEEK composites, but the UTS can be similar to that of compression molded PEEK after the microwave post processing for the flat and edge-on build orientations [55]. The mechanical properties of PEEK and carbon-fiber PEEK composites are dependent upon the crystallinity of the PEEK, which can be controlled by details of the processing [55].

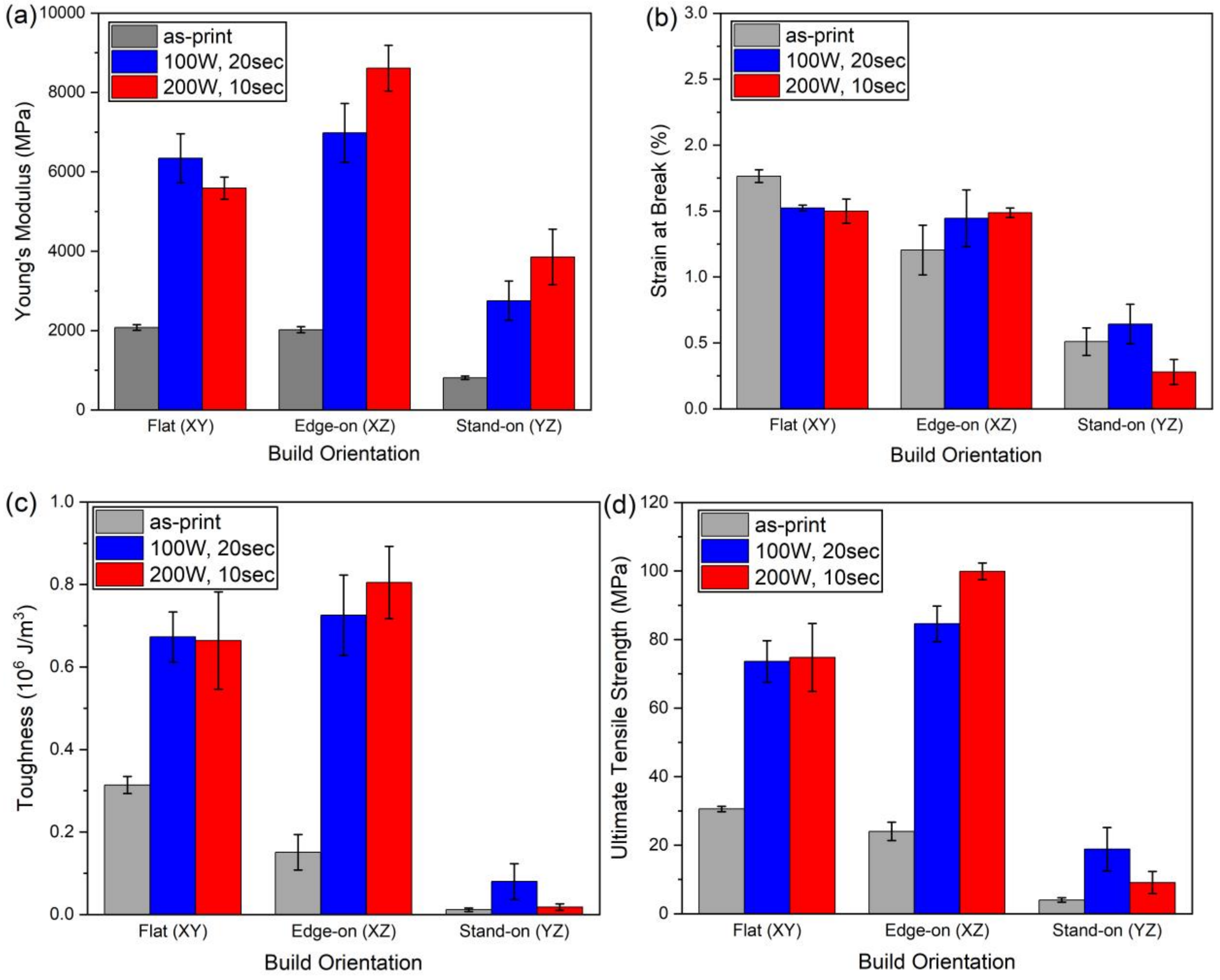

Figure 3. Influence of microwave post processing on the (a) elastic modulus, (b) strain at break, (c) toughness and (d) ultimate tensile strength as a function of print orientation and post-processing conditions.

3.3 Changes in crystallinity and crystal size of PEEK with microwave post-processing. To explain the enhancement in the mechanical performance with microwave post-processing, the most obvious rationale is an increase in the crystallinity of the specimens. It is known that crystallinity can significantly impact the mechanical properties of carbon-PEEK composites with traditional plastic manufacturing [55]. An increase in crystallinity tends to increase the elastic modulus and UTS, but decrease the fracture toughness [55]. However as shown in Figure 4a, the enthalpy of melting decreases with the microwave post processing for the flat build orientation. Interestingly, the crystallinity marginally increases in the as-printed state relative to the initial filament. These changes in crystallinity are related to the thermal and flow history. The melting point is essentially unchanged by post-processing with microwaves, so there is not a change to substantially smaller crystals that would exhibit lower melting points due to Gibbs-Thomson. As shown in Figure 4b, the changes in crystallinity are, in general, small with the crystallinity between 25 and 35% for the PEEK. This crystallinity is consistent with those typically observed for PEEK in 3D printing [56] as well as the crystallinity obtained from more traditional processing with compression molding (16-39%) [55]. To understand variability within the filament, four different locations of the cPEEK filament were examined by DSC. The result in Figure S7 shows near constant crystallinity of the PEEK (33.1 ± 0.7 %). These data indicate that simply improvements in the crystallinity are not responsible for the significant increase in the mechanical performance of the carbon-PEEK composites after microwave post-processing. The general decrease in crystallinity with microwave post-processing indicates that the crystals partially melt. If recrystallization increases the number of crystals with chains that bridge between roads, this would increase the strength of the interfaces and thus improve the mechanical performance of the printed specimens.

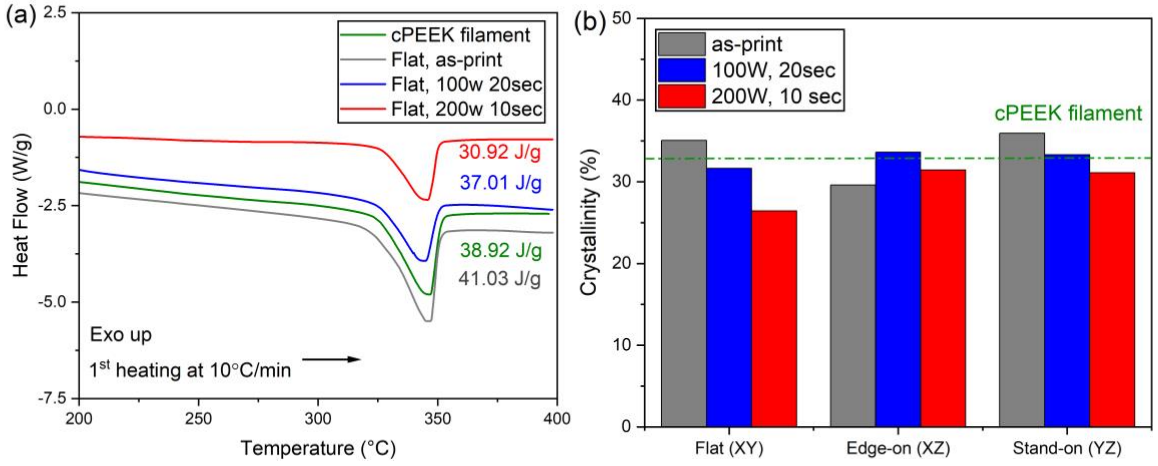

Figure 4. (a) DSC 1st heating curve of cPEEK filament, as-print and microwave post-processing samples in gauge region with specific heat of fusion (Note: the heat of fusion listed includes the mass of PEEK and carbon). (b) Calculated crystallinity of PEEK in the printed specimens based on 10 wt% carbon fiber in the composite.

This knowledge about the crystallinity of the printed specimens can be used to place the mechanical performance illustrated in Figure 3 in perspective to pure PEEK processed by compression molding with similar crystallinity. In this case, the UTS for the microwaved flat and edge-on samples is approaching that of pure PEEK from compression molding with 33%

crystallinity (97 MPa) [55]. The carbon fiber filler in the 3D printed parts leads to increased Young's modulus after microwave processing for the flat and edge-on build orientations in comparison to pure PEEK (4400 MPa) with 33% crystallinity. This indicates that the specimens with the flat and edge-on build orientation would exhibit performance that could directly replace PEEK produced with conventional manufacture.

X-ray diffraction provides additional insights into the impact of the microwave post-processing on the crystal structure of the PEEK. Figure 5 illustrates the x-ray diffraction profiles for the different build orientations and post processing with microwaves. The peak locations in the profiles are consistent with typical semicrystalline PEEK with an orthorhombic cell and the following assignments: (110) ~19°, (111) ~21°, (200) ~23°, and (211) ~28° [57, 58]. The peak near 26° is attributed to the crystallographic plane for the graphene stacks in the carbon fibers in the composite [59]. There are some clear differences in the diffraction profiles that depend both on the build orientation and post processing. Crystallization is dependent on shear and temperature history, so this dependence can explain the build orientation effect on the diffraction profiles. The observable peaks in the as-printed specimen changes with build orientation due to the effective orientation of the crystals. This orientation of the crystals is likely attributable to chain elongation during printing that does not relax quickly [13, 14]. Chain orientation is known to impact performance of 3D printed plastics [60, 61] with highly oriented chains reducing interdiffusion and interfacial strength development especially for glassy polymers [14, 62]. For semicrystalline polymers, the orientation of chains can improve crystallization through flow induced crystallization [63] and crystallization across the interface between printed road tends to be sufficient to provide weld strength rather than diffusion to form entanglements [30]. Thus, chain orientation may increase or decrease the mechanical performance for the PEEK depending on how this influences the local crystallization at the interface between roads. The chain orientation also leads to residual stress in the material that can lead to deformation after post-process annealing as the stress is relieved.

After microwave post-processing, the diffraction profile is also changed. In general, the peak width broadens after microwave post-processing; the peak width is inversely proportional to the crystal size through the Scherrer equation [64]. The crystal size is generally correlated with fracture mechanics with a more brittle specimen expected as the PEEK crystal size increases [65]. Table 1 summarizes the average crystal size with respect of build orientation and microwave post-processing conditions. Detailed information regarding the peak position and full width at half maximum (FWHM) at each processing condition can be found in Tables S1-S9. These data indicate that the microwave post-processing as used in this study does not lead to an average increase in the size of the PEEK crystals. The post-processing decreases the crystal size on average, which indicates that the PEEK is at least partially melted by the microwave processing. Thus, the post-processing with microwaves is producing actions (lower crystallinity, smaller crystal size) that tend to reduce the mechanical performance of 3D printed PEEK when comparing as-printed parts [56].

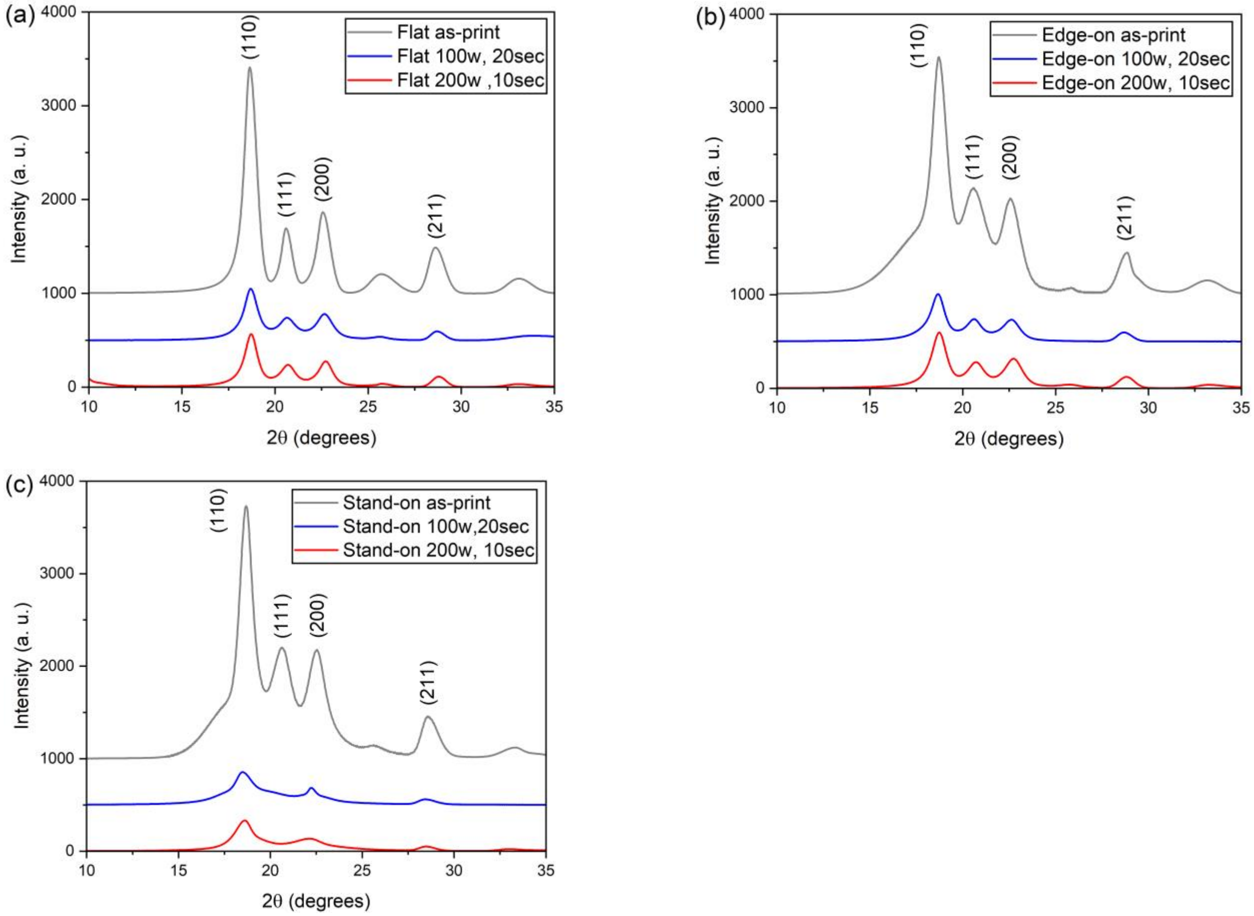

Figure 5. XRD profiles with different post-processing for the (a) Flat, (b) Edge-on and (c) Stand-on build orientations. The profiles are vertically offset for clarity.

Table 1. Influence of build orientation and microwave post-processing conditions on the average crystal size of PEEK from Scherrer analysis of XRD data.

Processing condition	Average crystal size (nm)
Flat as-printed	10.49
Flat 100 W, 20 s	8.40
Flat 200 W, 10 s	8.94
Edge-on as-printed	7.60
Edge-on 100 W, 20 s	7.70
Edge-on 200 W, 10 s	7.59
Stand-on as-printed	7.43
Stand-on 100 W, 20 s	6.37
Stand-on 200 W, 10 s	7.46

3.4 Dimensional accuracy and internal microstructure.

There is evidence from XRD and DSC that some PEEK crystals melt during the microwave processing, so it is important to understand if there is significant loss of the dimensional accuracy of the parts with the post processing. Figure 6 illustrates the 3D structure of the printed tensile bars as a function of post-processing conditions. Inaccuracies in the as-printed specimen are primarily near the ends of the tensile bar, which can be attributed to a small but resolvable bend to the tensile bar (Figure 6a). In general, the structure is well maintained through the microwave post-processing used, but there are some local regions that appear to have formed bubbles or blisters on the surface of the printed part. These could be associated with trapped outgassing as the specimen is rapidly heated. These defects appear to be localized primarily to the middle of the gauge region of the tensile bars near the edges. This localization of the defects is indicative of the non-uniform heating of the printed samples by the microwaves. In addition to these defects, the bend of the tensile bar increases in comparison to the as-printed sample with the curvature increasing in the same direction as the original warp of the tensile bar after microwave post-processing (Figure 6b and 6c). This increase in the warpage could be associated with some stress relaxation that bends the sample. In addition to this warpage, careful examination of the 3D scan reconstruction shows that the thickness of the sample does increase slightly with a maximum of 10% increase outside of the regions with blisters. However, the overall dimensions of the specimens does not dramatically change as has been found in some cases with other composites when annealing at high temperatures with conventional thermal oven [66].

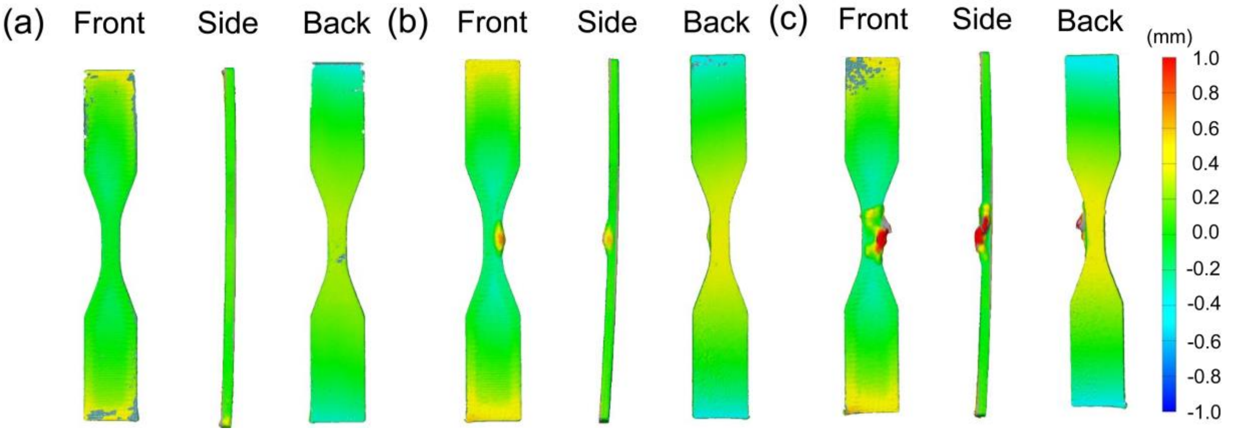

Figure 6. Comparison of the structure of the 3D printed carbon PEEK with flat build orientation (a) without microwaves, and after (b) 100 W, 20 s and (c) 200 W, 10 s microwave post-processing.

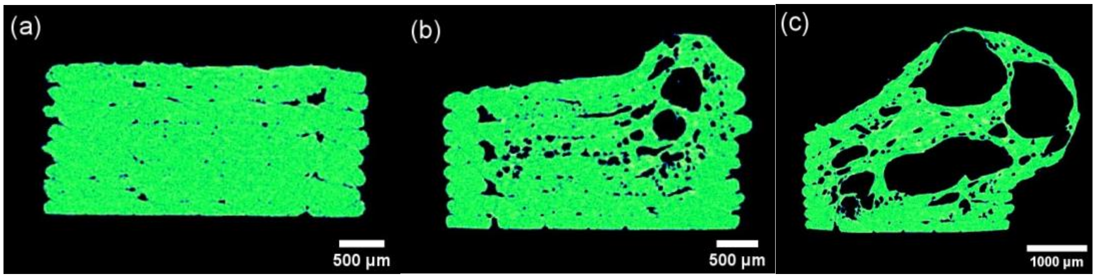

Figure 7. 2D cross-section cuts from the 3D reconstruction of the gauge region from low resolution µCT scans for flat orientation. The impact of post-processing conditions on the structure are evident when comparing the (a) as printed specimen with ones post-processed at (b) 100 W, 20 s and (c) 200W, 10 s with microwaves. The cross-sections are specifically located in the gauge

region where the blisters occurred after microwave post-processing to best illustrate the structure associated with the blisters. Other regions show limited differences between these three post-processing conditions.

For a more detailed insight into the structural differences, μCT was used to examine the 3D structure of the gauge region as shown in Figure 7. From examination of the internal structure with μCT, the surface protrusions observed with the 3D blue light scans in Figure 6 are shown to be larger voids in the printed parts. The microwave post-processing produces some larger voids in the parts within the gauge region. According to FTIR analysis for all specimens shown in Figure S8, there are limited changes in the spectra in comparison to the cPEEK filament, which suggests during the selected microwave post-processing is limited. The only outlier is the specimen with flat build orientation and 100W 20s microwave post-processing where a broad peak between 3000-3500 cm^{-1} evolved. This broad peak is generally associated with -OH stretching bond, which could be associated with some oxidation and/or adsorbed water. This also leads to our hypothesis for the void formation, which is insufficient drying of the larger printed objects when compared to typical filament drying protocols. The adsorbed water in PEEK will expand significantly on heating to foam the sample if the temperature exceeds T_g of the PEEK. Typically, heating is slow, so water can evaporate and leave the system prior to reaching T_g, but the rapid heating rate associated with the microwaves limits the loss of water from the PEEK [67]. These voids in the printed parts would be expected to embrittle the cPEEK, but the microwave processing tends to not significantly impact the strain at break (Figure 3b).

Examination of the failure surfaces after the tensile test can provide some additional insights into the microwave mechanism for enhanced mechanical performance. Figure 8 illustrates the cross-sections of the fracture surfaces. For the flat build orientation, the deformation of the tensile bar does not appear to significantly influence the general geometry of the cross-section. Without microwave post-processing (Figure 8a), the printed roads can still be resolved within the fracture area. Exposure to 200 W microwaves leads to marked changes in the structure of the fracture surface as shown in Figure 8b. The rectangular cross-section expected for the tensile bar specimen is deformed, but this was prior to deformation. Examination of the SEM micrograph reveals large pores in the deformed region. It is striking that the ultimate tensile strength of the highly porous specimen (Figure 8b) is more than 3 times that of the as printed specimen (Figure 8a). However, the discrete roads within the printed specimens are not as clearly defined after microwave post-processing. When printed in the stand-on build orientation, plastic deformation occurs at the edge of the specimen as the sample fully fractures. Similar structures at the surface are found for the stand-on build orientation without (Figure 8c) and with (Figure 8d) microwave postprocessing. There also appears to be less porosity after microwave post-processing when comparing the micrographs for the specimens printed in the stand-on build orientation, which is counter to the images of the flat build orientation.

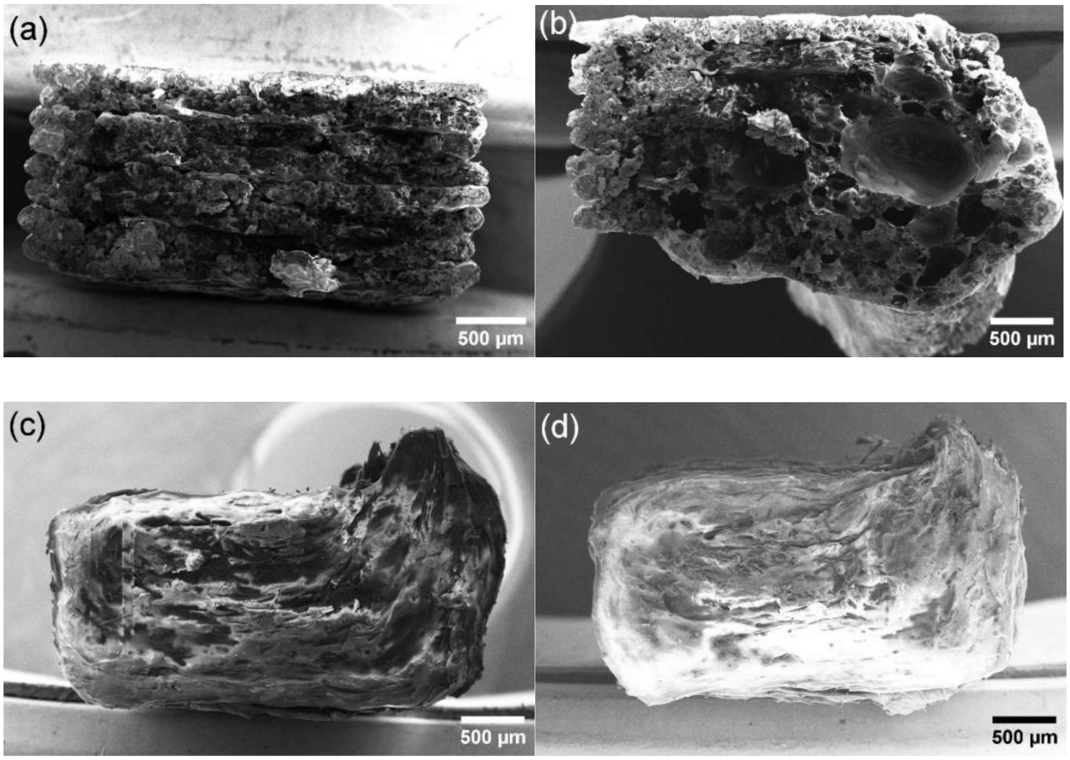

Figure 8. SEM micrographs of the fracture surfaces for the flat build orientation (a) without and (b) with microwave postprocessing (200 W, 10 s) and the stand-on build orientation (c) without and (d) with microwave postprocessing (200 W, 10 s)

To better understand porosity introduced by the microwave post-processing, µCT images of the printed specimens were examined to determine the void fraction as well as the distribution in the pore size. These µCT images are included in the appendix (Figure S9). In general, when examining 3D printed plastics, increases in the void fraction printed parts tends to decrease the mechanical performance [68, 69] of 3D printed parts. However as shown in Figure 9a, the void fraction is significantly increased with the microwave processing. The highest porosity was found for the flat build orientation with 100 W microwave post processing, but this post-processing leads to a factor of nearly four increase in the modulus and ultimate tensile strength. Consistent with the previous observations for the fracture surfaces, there is limited difference in the porosity for the specimens printed in the stand-on build orientation. However, there is a disconnect between the porosity of these cPEEK specimens and their mechanical performance after microwave post-processing. The differences in the porosity are suggestive of a gas expansion process during the microwave heating as the longer microwave exposure, although at a lower power, tends to lead to a greater increase in the porosity.

To better understand the changes in the void fraction, the void size distribution was determined from the μCT images. The distribution in void sizes tends to only modestly shift to larger size with the microwave processing (Figure 9b-d) except in the case of the flat build orientation after 100 W microwaves (Figure 9b). With this one case, there was a significant shift in the pore size distribution to larger pores with a loss in the smallest pores measurable by μCT. Even with the small increase in pore size on average, there is a substantial increase in the overall porosity for the flat and edge-on build orientations. As the larger pores contribute more to the void fraction on a per pore basis, these small changes in the distribution can lead to appreciable increases in the overall porosity of the specimens. For the stand-on orientation, the shift in the pore size distribution is small (Figure 9d), which is consistent with the limited increase in the overall porosity with microwave post-processing with this build orientation. These results are consistent with the increased porosity being associated with gaseous expansion during the microwave processing.

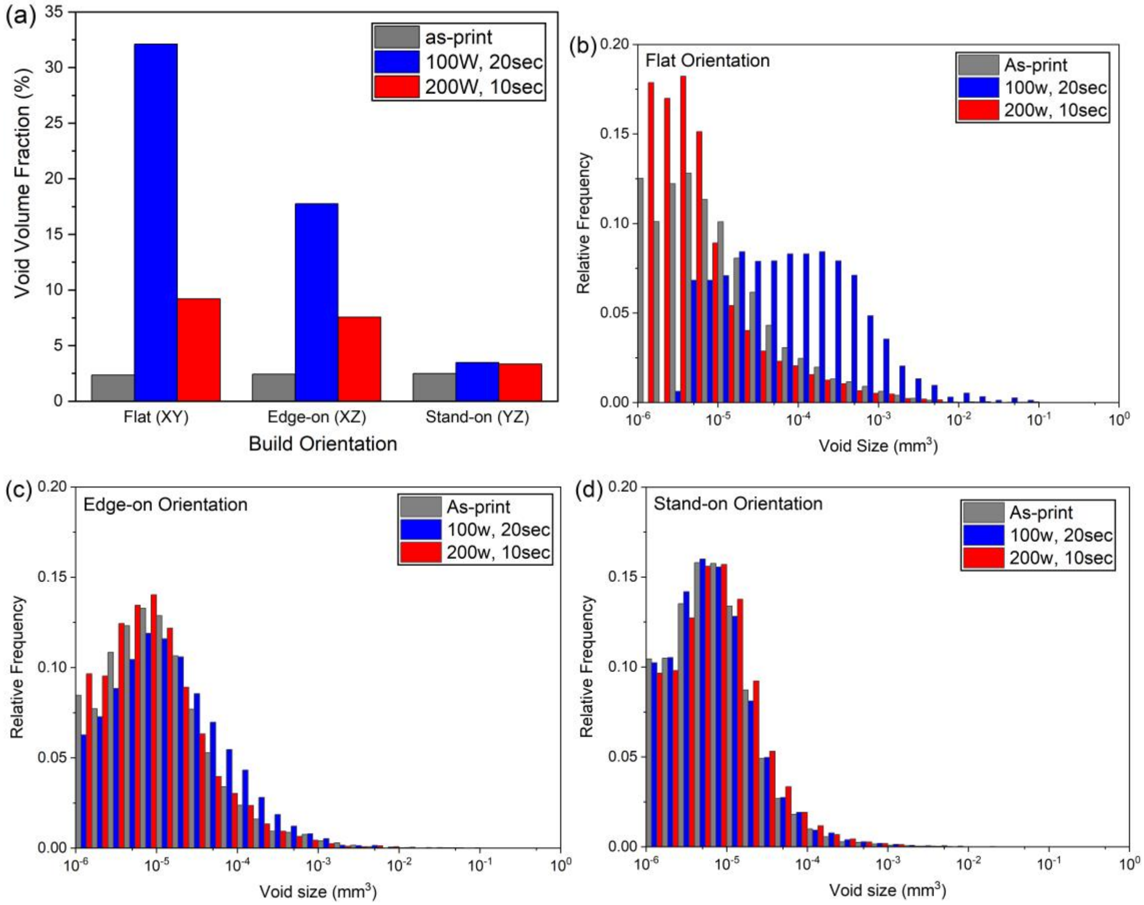

Figure 9. (a) Void fraction as a function of the build orientation and microwave post-processing conditions. Histograms of void size distribution from analysis of μCT images for (b) flat, (c) edge-on and (d) stand-on build orientations.

As the mechanical properties and the structural changes from the microwave post-processing appear to be dependent on the build orientation, it is instructive to consider the microwave interactions with the printed object to enable the heating and how this heating process could depend on the spatial arrangement of the carbon fibers. Carbonaceous materials are known as strong absorbers for local heating to promote chemistry with microwaves [70]. Microwave heating with carbons generally occurs through the interaction between microwaves and the electrons through interfacial (Maxwell-Wagner-Sillars) polarization and Joule heating. However, the anisotropy of the carbon fibers means that the orientation of the fibers within the printed part may influence the heating.

Figure 10a illustrates a higher resolution μCT image of a printed sample after microwave post-processing. The difference in the electron density between PEEK and the carbon fiber enables visualization of the distribution of filler in the printed part. There is orientation of the fibers in the flow direction with the side and end view of the fibers clearly observed in the alternating layers with 0° and 90° orientation for the raster. Figure 10c illustrates schematically the relationship between the print path and observed orientation of the carbon fibers. The extent of orientation can be quantified by examining all of the fibers in the field of single print line and determining orientation angle relative to the print direction. The selected region for the fiber orientation analysis is shown in Figure S10. This region was used to confirm the carbon fiber loading in the filament. From the μCT, printed filament contains 7.96 vol% carbon fiber, which based on the reported densities of carbon fiber and PEEK leads to a composite containing 11.2 wt% carbon fiber. This is similar to the reported 10 wt% carbon fiber loading for the composite. As shown in Figure 10b, most of the carbon fibers are oriented in the flow direction. The Herman's orientation factor determined from this distribution is 0.8857, which is indicative of a high degree of orientation of the carbon fibers after printing. As the print path for the roads will impact the relative distribution of carbon fibers in the object, this difference may account for some of the differences in the changes in properties with microwave post-processing that depends on the build orientation.

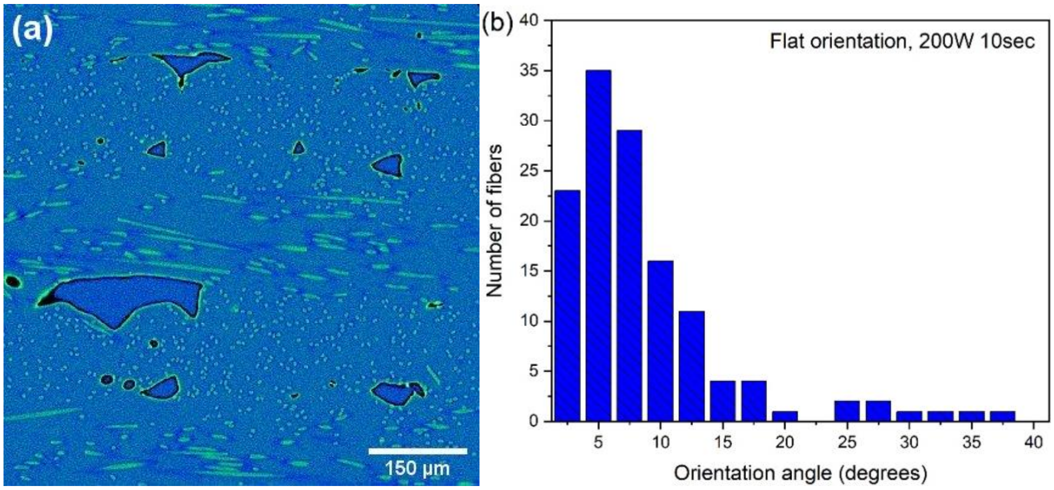

(c)

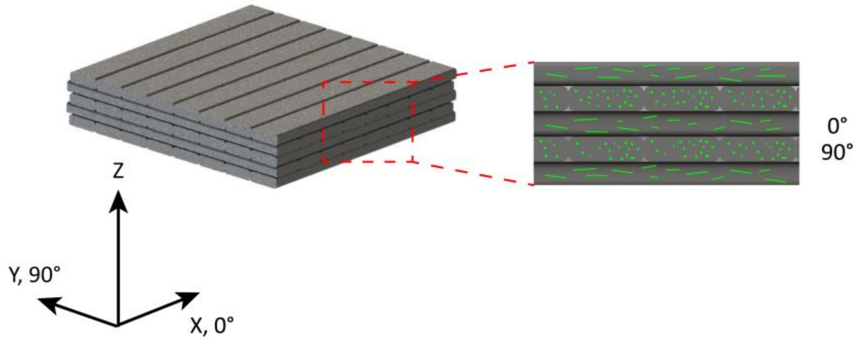

Figure 10. (a) μCT image with 700 nm resolution scan for fiber orientations of flat build orientation specimen after 200 W, 10 s microwaves. (b) Single layer fiber orientation angle analysis base on the printing direction. (c) Schematic illustrating the relationship of the μCT imaged area shown to the print path.

Similarly, the as print specimens were also examined with high resolution μCT for carbon fiber orientation. As shown in Figure 11, the carbon fibers tilt angle along with print direction are presented in relative frequency within fixed space of a single layer. For flat and edge-on build orientation, nearly all of the carbon fibers are aligned with print direction with the tilt angle less than 50 degrees. In contrast, fiber orientation angle from the stand-on build orientation specimen is not highly correlated with the print direction. This difference is not due to the shorter path length leading to the fibers not aligning as the fiber orientation for the cPEEK filament is the highest alignment among four specimens examined. Instead we attribute the lower orientation of the carbon fibers within the stand-on build orientation specimen to the shear stresses experienced during the printing process. The short road length in the stand-on build orientation leads to near continuous changes in the shear rate as the print head initially accelerates as the road starts and decelerates as the end of the road is approached. The reduced orientation in cases with signifiacnt acceleration and deceleration is consistent with the challenges with orienting fibers in start-up and other transient flows [71].

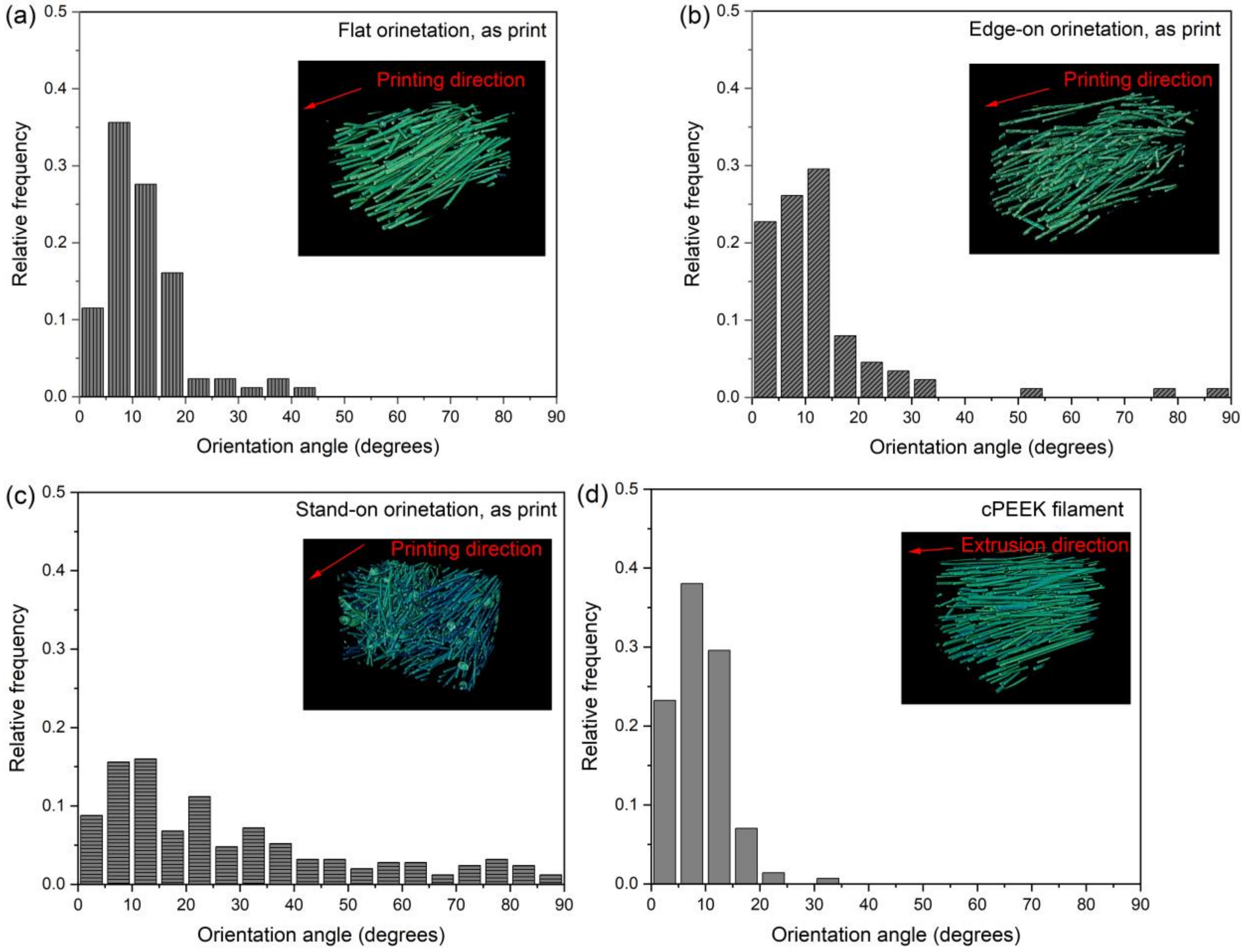

Figure 11. µCT image (inset) with 700 nm resolution scan to determine the carbon fiber orientation histograms for (a) flat build orientation, (b) edge-on build orientation, and (c) stand-on build orientation specimen as printed. (d) The same analysis is applied to the cPEEK filament for reference.

To provide a more quantitative comparison, Table 2 summarizes the Herman's orientation factor for the carbon fiber in the PEEK. 3D printing for all conditions examined leads to decreased orientation of the carbon fibers. There is a significant decrease in the Herman's orientation factor from flat to edge-on to stand-on build orientation. Due to the high dielectric loss of carbon fiber, the misalignment of carbon fibers can cause microwave deflection and reduction in the heating efficiency [38, 72]. Additionally, the coupling of the microwave depends on the length of the carbon fiber [73]. Due to the long relative wavelength of microwaves in comparison to the length of the carbon fibers, orientated fibers that touch effectively increases the apparent carbon fiber length to enhance the heating. For flat and edge-on build orientation specimens, the fibers tend to be mostly orientated in the same direction and a significant fraction of the fibers appear to be in contact. This contrasts with the stand-on build orientation with less orientated carbon fibers, where the effective length of a carbon fiber is not significantly increased. These differences in carbon fiber morphology in the printed parts is consistent with both the decreased mechanical properties (Figure 3) and porosity (Figure 8) with microwave post-processing with the stand-on orientation. Similarly, the flat print orientation exhibits larger Herman's orientation factors and leads to the post pronounced decrease in crystallinity and crystal size. In addition to the original orientation for the carbon fibers, the fiber orientation was also examined for the flat build orientation after microwave post-processing. As shown in Table 2, the Herman's orientation factor was not systematically increased or decreased. As different specimens were examined, we are unable to determine if there was a change in the orientation on microwave processing or if this was a result of variability in the original printed structure. The later could explain the relatively large variance in the tensile response in the microwave post-processed specimens.

Table 2. Summary of Herman's orientation factor for different build orientation and microwave condition.

Processing condition	Herman's orientation factor
cPEEK filament	0.925
Flat as-printed	0.847
Flat 100 W, 20 s	0.682
Flat 200 W, 10 s	0.886
Edge-on as-printed	0.697
Stand-on as-printed	0.274

These results demonstrate the importance of the orientation of the carbon fibers in the heating by the microwaves, which leads to significant increases in the mechanical properties of the 3D printed carbon-PEEK. Moreover, the largest increases in modulus and UTS tend to be found for specimens with larger increase in porosity, which is counter to established effect of voids on mechanical performance [74]. Additionally, the crystallinity of PEEK is known to be directly correlated with elastic modulus and UTS [55], but the crystallinity of the specimens is not increased on microwave post-processing and decreases slightly in some cases. These results point to a re-crystallization across the interface between printed roads as the origin of the increased mechanical performance with the microwave post-processing.

4. CONCLUSIONS

Efficient coupling of microwaves by the carbon fibers in a PEEK composite enable the effective post-processing of 3D printed carbon-PEEK composites to dramatically increase the mechanical performance of the printed parts with commercial filaments, even in the absence of segregation of the carbon fillers to the interfaces as has been used in prior works [23]. In this work, the printed specimen can deform significantly or even degrade at high microwave power or long post processing times, so knowledge of the appropriate processing window is critical to observe improvements in performance. Short exposures (10-20 s) at 100 W or 200 W leads to 250-400% increase in elastic modulus, irrespective of build orientation. Despite this large increase in modulus, the average crystallinity does not increase, nor does the average crystal size from this post processing. We attribute the improvement in mechanical properties to improvements between adjacent printed roads from the microwave post processing, which allows for some relaxation of chain orientation and formation of crystals across the interface. This work points to the importance of understanding interfaces between printed roads. Future work will focus on more quantitatively elucidating the local changes in crystal morphology to better understand how this local structure controls the mechanical response in 3D printed parts. Unlike glassy polymers where reptation across the interface has been deemed critical to strong interfaces [8, 62, 75], but is difficult to experimentally observe [20], the crystal motifs provide readily observable morphological features that can be quantitatively assessed [63, 76]. More generally, this simple post processing strategy should be applicable to a variety of carbon filled composites based on semicrystalline polymers that are commonly used in MatEx 3D printing to enable significant improvements in the mechanical performance for additive manufacture with appropriate postprocessing conditions based on microwave power and time.

Declaration of Competing Interest

The authors declare that they have no known competing financial interests or personal relationships that could have appeared to influence the work reported in this paper.

Acknowledgments

This work was supported by the National Science Foundation (NSF, grant numbers CMMI-2011289 and CBET- 1510612). This work utilized facilities within the Center for Quantitative Image (CQI) in the Institutes of Energy and the Environment at The Pennsylvania State University. The authors thank Timothy Stecko and Whitney Yetter for their assistance with μCT data collection and analyses. The authors also acknowledge the assistance of Andrew Knoll for the XRD measurements.

References

[1] A. Marzola, E. Mussi, F. Uccheddu, 3D Printed Materials for High Temperature Applications, Design Tools and Methods in Industrial Engineering, Adm 2019 (2020) 936-947.
[2] W. Gao, Y.B. Zhang, D. Ramanujan, K. Ramani, Y. Chen, C.B. Williams, C.C.L. Wang, Y.C. Shin, S. Zhang, P.D. Zavattieri, The status, challenges, and future of additive manufacturing in engineering, Comput.-Aided Des. 69 (2015) 65-89.
[3] L.E.J. Thomas-Seale, J.C. Kirkman-Brown, M.M. Attallah, D.M. Espino, D.E.T. Shepherd, The barriers to the progression of additive manufacture: Perspectives from UK industry, International Journal of Production Economics 198 (2018) 104-118.
[4] S.E. Zeltmann, N. Gupta, N.G. Tsoutsos, M. Maniatakos, J. Rajendran, R. Karri, Manufacturing and Security Challenges in 3D Printing, Jom 68(7) (2016) 1872-1881.
[5] A. Garcia-Dominguez, J. Claver, M.A. Sebastian, Optimization Methodology for Additive Manufacturing of Customized Parts by Fused Deposition Modeling (FDM). Application to a Shoe Heel, Polymers 12(9) (2020) 30.
[6] V. Vijayaraghavan, A. Garg, J.S.L. Lam, B. Panda, S.S. Mahapatra, Process characterisation of 3D-printed FDM components using improved evolutionary computational approach, Int. J. Adv. Manuf. Technol. 78(5-8) (2015) 781-793.
[7] O.A. Mohamed, S.H. Masood, J.L. Bhowmik, Optimization of fused deposition modeling process parameters: a review of current research and future prospects, Adv. Manuf. 3(1) (2015) 42-53.

[8] J. Bartolai, T.W. Simpson, R.X. Xie, Predicting strength of additively manufactured thermoplastic polymer parts produced using material extrusion, Rapid Prototyping Journal 24(2) (2018) 321-332.

[9] C.S. Davis, K.E. Hillgartner, S.H. Han, J.E. Seppala, Mechanical strength of welding zones produced by polymer extrusion additive manufacturing, Addit. Manuf. 16 (2017) 162-166.

[10] M. Spoerk, F. Arbeiter, H. Cajner, J. Sapkota, C. Holzer, Parametric optimization of intra- and inter-layer strengths in parts produced by extrusion-based additive manufacturing of poly(lactic acid), Journal of Applied Polymer Science 134(41) (2017) 15.

[11] T.J. Coogan, D.O. Kazmer, Prediction of interlayer strength in material extrusion additive manufacturing, Additive Manufacturing 35 (2020) 17.

[12] A. Das, E.L. Gilmer, S. Biria, M.J. Bortner, Importance of Polymer Rheology on Materials Extrusion Additive Manufacturing: Correlating Process Physics to Print Properties, ACS Applied Polymer Materials 3(3) (2021) 1218-1249.

[13] C. McIlroy, P.D. Olmsted, Deformation of an amorphous polymer during the fused-filament-fabrication method for additive manufacturing, Journal of Rheology 61(2) (2017) 379-397.

[14] A. Costanzo, R. Spotorno, M.V. Candal, M.M. Fernandez, A.J. Mueller, R.S. Graham, D. Cavallo, C. McIlroy, Residual alignment and its effect on weld strength in material-extrusion 3D-printing of polylactic acid, Additive Manufacturing 36 (2020) 101415.

[15] A. El Magri, K. El Mabrouk, S. Vaudreuil, M.E. Touhami, Experimental investigation and optimization of printing parameters of3Dprinted polyphenylene sulfide through response surface methodology, Journal of Applied Polymer Science 138(1) (2021).

[16] E. Gkartzou, E.P. Koumoulos, C.A. Charitidis, Production and 3D printing processing of bio-based thermoplastic filament, Manufacturing Review 4 (2017).

[17] T. D'Amico, A.M. Peterson, Bead parameterization of desktop and room-scale material extrusion additive manufacturing: How print speed and thermal properties affect heat transfer, Additive Manufacturing 34 (2020).

[18] G. Cicala, G. Ognibene, S. Portuesi, I. Blanco, M. Rapisarda, E. Pergolizzi, G. Recca, Comparison of Ultem 9085 Used in Fused Deposition Modelling (FDM) with Polytherimide Blends, Materials 11(2) (2018).

[19] D.S. Simmons, M.T. Cicerone, Q. Zhong, M. Tyagi, J.F. Douglas, Generalized localization model of relaxation in glass-forming liquids, Soft Matter 8(45) (2012) 11455-11461.

[20] G. Agrawal, R.P. Wool, W.D. Dozier, G.P. Felcher, J. Zhou, S. Pispas, J.W. Mays, T.P. Russell, Interdiffusion of polymers across interfaces, Journal of Polymer Science Part B-Polymer Physics 34(17) (1996) 2919-2940.

[21] E.O. Bachtiar, V.C. Ritter, K. Gall, Structure-property relationships in 3D-printed poly (L-lactide-co-epsilon-caprolactone) degradable polymer, Journal of the Mechanical Behavior of Biomedical Materials 121 (2021).

[22] R.A. Giordano, B.M. Wu, S.W. Borland, L.G. Cima, E.M. Sachs, M.J. Cima, Mechanical properties of dense polylactic acid structures fabricated by three dimensional printing, Journal of Biomaterials Science-Polymer Edition 8(1) (1996) 63-75.

[23] C.B. Sweeney, B.A. Lackey, M.J. Pospisil, T.C. Achee, V.K. Hicks, A.G. Moran, B.R. Teipel, M.A. Saed, M.J. Green, Welding of 3D-printed carbon nanotube-polymer composites by locally induced microwave heating, Science Advances 3(6) (2017).

[24] C.B. Sweeney, M.L. Burnette, M.J. Pospisil, S.A. Shah, M. Anas, B.R. Teipel, B.S. Zahner, D. Staack, M.J. Green, Dielectric Barrier Discharge Applicator for Heating Carbon Nanotube-

Loaded Interfaces and Enhancing 3D-Printed Bond Strength, Nano Letters 20(4) (2020) 2310-2315.

[25] N. Patil, A.C. Camacho, N.K. Mishra, P. Singhla, C.B. Sweeney, M.A. Saed, M. Radovic, M.J. Green, Radio Frequency and Microwave Heating of Preceramic Polymer Nanocomposites with Applications in Mold-Free Processing, Advanced Engineering Materials 21(8) (2019).

[26] N.Y. Li, G. Link, J. Jelonnek, 3D microwave printing temperature control of continuous carbon fiber reinforced composites, Composites Science and Technology 187 (2020).

[27] N.Y. Li, G. Link, J. Jelonnek, Rapid 3D microwave printing of continuous carbon fiber reinforced plastics, Cirp Annals-Manufacturing Technology 69(1) (2020) 221-224.

[28] Q.J. Ding, J.C. Fan, G. Zhao, Effect of protective atmosphere and secondary treatment on filament fusion of polylactic acid composites prepared by fused deposition modeling, Journal of Applied Polymer Science 139(12) (2022).

[29] D.P. Street, A.H. Mah, W.K. Ledford, S. Patterson, J.A. Bergman, B.S. Lokitz, D.L. Pickel, J.M. Messman, G.E. Stein, S.M. Kilbey, Tailoring Interfacial Interactions via Polymer-Grafted Nanoparticles Improves Performance of Parts Created by 3D Printing, Acs Applied Polymer Materials 2(3) (2020) 1312-1324.

[30] J.R. Ai, B.D. Vogt, Size and print path effects on mechanical properties of material extrusion 3D printed plastics, Progress in Additive Manufacturing (2022) in press.

[31] C.A. Chatham, C.E. Zawaski, D.C. Bobbitt, R.B. Moore, T.E. Long, C.B. Williams, Semi-Crystalline Polymer Blends for Material Extrusion Additive Manufacturing Printability: A Case Study with Poly(ethylene terephthalate) and Polypropylene, Macromolecular Materials and Engineering 304(5) (2019).

[32] M. Spoerk, C. Holzer, J. Gonzalez-Gutierrez, Material extrusion-based additive manufacturing of polypropylene: A review on how to improve dimensional inaccuracy and warpage, J. Appl. Polym. Sci. 137(12) (2020) 16.

[33] A. Gudadhe, N. Bachhar, A. Kumar, P. Andrade, G. Kumaraswamy, Three-Dimensional Printing with Waste High-Density Polyethylene, ACS Appl. Polym. Mater. 1(11) (2019) 3157-3164.

[34] A. Das, A.E.C. Marnot, J.J. Fallon, S.M. Martin, E.G. Joseph, M.J. Bortner, Material Extrusion-Based Additive Manufacturing with Blends of Polypropylene and Hydrocarbon Resins, ACS Appl. Polym. Mater. 2(2) (2020) 911-921.

[35] X. Wang, M. Jiang, Z.W. Zhou, J.H. Gou, D. Hui, 3D printing of polymer matrix composites: A review and prospective, Compos. Pt. B-Eng. 110 (2017) 442-458.

[36] A. Costanzo, D. Cavallo, C. McIlroy, High-performance co-polyesters for material-extrusion 3D printing: A molecular perspective of weld properties, Additive Manufacturing 49 (2022).

[37] W.H. Chen, X.L. Zhang, D. Tan, P. Xu, B.S. Yang, K. Shi, B. Zhu, Q. Liu, Y.F. Lei, S. Liu, L.J. Xue, Improvement in Mechanical Properties of 3D-Printed PEEK Structure by Nonsolvent Vapor Annealing, Macromolecular Rapid Communications 43(7) (2022).

[38] J. Galos, Microwave processing of carbon fibre polymer composites: a review, Polymers and Polymer Composites 29(3) (2021) 151-162.

[39] D.E. Clark, W.H. Sutton, Microwave processing of materials, Annual Review of Materials Science 26 (1996) 299-331.

[40] H.Y. Qiao, M.T. Saray, X.Z. Wang, S.M. Xu, G. Chen, Z.N. Huang, C.J. Chen, G. Zhong, Q. Dong, M. Hong, H. Xie, R. Shahbazian-Yassar, L.B. Hu, Scalable Synthesis of High Entropy Alloy Nanoparticles by Microwave Heating, Acs Nano 15(9) (2021) 14928-14937.

[41] Y.V. Bykov, K.I. Rybakov, V.E. Semenov, High-temperature microwave processing of materials, Journal of Physics D-Applied Physics 34(13) (2001) R55-R75.

[42] P. Blyweert, V. Nicolas, V. Fierro, A. Celzard, 3D printing of carbon-based materials: A review, Carbon 183 (2021) 449-485.

[43] A.A. Mehmetalkan, J.N. Hay, THE CRYSTALLINITY OF POLY(ETHER ETHER KETONE), Polymer 33(16) (1992) 3527-3530.

[44] Z. Qiang, C.H. Ye, K.H. Lin, M.L. Becker, K.A. Cavicchi, B.D. Vogt, Evolution in Surface Morphology During Rapid Microwave Annealing of PS-b-PMMA Thin Films, Journal of Polymer Science Part B-Polymer Physics 54(15) (2016) 1499-1506.

[45] G.A. Tompsett, W.C. Conner, K.S. Yngvesson, Microwave synthesis of nanoporous materials, Chemphyschem 7(2) (2006) 296-319.

[46] D.W. Collinson, N. Von Windheim, K. Gall, L.C. Brinson, Direct Evidence of Interfacial Crystallization Preventing Weld Formation During Fused Filament Fabrication of Poly(ether ether ketone), Addit. Manuf. (2022) 102604.

[47] N. Devi, S. Sahoo, R. Kumar, R.K. Singh, A review of the microwave-assisted synthesis of carbon nanomaterials, metal oxides/hydroxides and their composites for energy storage applications, Nanoscale (2021) doi: 10.1039/D1NR01134K.

[48] Y. Nakagawa, K. Mori, T. Maeno, 3D printing of carbon fibre-reinforced plastic parts, International Journal of Advanced Manufacturing Technology 91(5-8) (2017) 2811-2817.

[49] M. Spoerk, C. Savandaiah, F. Arbeiter, G. Traxler, L. Cardon, C. Holzer, J. Sapkota, Anisotropic properties of oriented short carbon fibre filled polypropylene parts fabricated by extrusion-based additive manufacturing, Compos. Pt. A-Appl. Sci. Manuf. 113 (2018) 95-104.

[50] S. Shaffer, K.J. Yang, J. Vargas, M.A. Di Prima, W. Voit, On reducing anisotropy in 3D printed polymers via ionizing radiation, Polymer 55(23) (2014) 5969-5979.

[51] C.G. Schirmeister, T. Hees, E.H. Licht, R. Mulhaupt, 3D printing of high density polyethylene by fused filament fabrication, Addit. Manuf. 28 (2019) 152-159.

[52] K. Yang, J.C. Grant, P. Lamey, A. Joshi-Imre, B.R. Lund, R.A. Smaldone, W. Voit, Diels-Alder Reversible Thermoset 3D Printing: Isotropic Thermoset Polymers via Fused Filament Fabrication, Advanced Functional Materials 27(24) (2017).

[53] P. Wang, B. Zou, S.L. Ding, C.Z. Huang, Z.Y. Shi, Y.S. Ma, P. Yao, Preparation of short CF/GF reinforced PEEK composite filaments and their comprehensive properties evaluation for FDM-3D printing, Composites Part B-Engineering 198 (2020).

[54] S.-L. Gao, J.-K. Kim, Cooling rate influences in carbon fibre/PEEK composites. Part 1. Crystallinity and interface adhesion, Composites Part A: Applied Science and Manufacturing 31(6) (2000) 517-530.

[55] M.F. Talbott, G.S. Springer, L.A. Berglund, THE EFFECTS OF CRYSTALLINITY ON THE MECHANICAL-PROPERTIES OF PEEK POLYMER AND GRAPHITE FIBER REINFORCED PEEK, Journal of Composite Materials 21(11) (1987) 1056-1081.

[56] C.C. Yang, X.Y. Tian, D.C. Li, Y. Cao, F. Zhao, C.Q. Shi, Influence of thermal processing conditions in 3D printing on the crystallinity and mechanical properties of PEEK material, J. Mater. Process. Technol. 248 (2017) 1-7.

[57] D.R. Rueda, F. Ania, A. Richardson, I.M. Ward, F.J.B. Calleja, X-RAY-DIFFRACTION STUDY OF DIE DRAWN POLY(ARYLETHERKETONE) (PEEK), Polymer Communications 24(9) (1983) 258-260.

[58] P.C. Dawson, D.J. Blundell, X-RAY DATA FOR POLY(ARYL ETHER KETONES), Polymer 21(5) (1980) 577-578.

[59] T. Nishino, H. Naito, K. Nakamura, K. Nakamae, X-ray diffraction studies on the stress transfer of transversely loaded carbon fibre reinforced composite, Composites Part a-Applied Science and Manufacturing 31(11) (2000) 1225-1230.

[60] N.M. Hassan, K.B. Migler, A.H.R. Walker, A.P. Kotula, J.E. Seppala, Comparing polarized Raman spectroscopy and birefringence as probes of molecular scale alignment in 3D printed thermoplastics, Mrs Communications 11(2) (2021) 157-167.

[61] R.H. Somani, B.S. Hsiao, A. Nogales, S. Srinivas, A.H. Tsou, I. Sics, F.J. Balta-Calleja, T.A. Ezquerra, Structure development during shear flow-induced crystallization of i-PP: In-situ small-angle X-ray scattering study, Macromolecules 33(25) (2000) 9385-9394.

[62] E.L. Gilmer, D. Anderegg, J.M. Gardner, G. Sauti, E.J. Siochi, S.H. McKnight, D.A. Dillard, C. McIlroy, M.J. Bortner, Temperature, diffusion, and stress modeling in filament extrusion additive manufacturing of polyetherimide: An examination of the influence of processing parameters and importance of modeling assumptions, Additive Manufacturing 48 (2021).

[63] L.A. Northcutt, S.V. Orski, K.B. Migler, A.P. Kotula, Effect of processing conditions on crystallization kinetics during materials extrusion additive manufacturing, Polymer 154 (2018) 182-187.

[64] U. Holzwarth, N. Gibson, The Scherrer equation versus the 'Debye-Scherrer equation', Nature Nanotechnology 6(9) (2011) 534-534.

[65] Y. Wang, B.L. Chen, K. Evans, O. Ghita, Enhanced Ductility of PEEK thin film with self-assembled fibre-like crystals, Scientific Reports 8 (2018).

[66] J. Butt, R. Bhaskar, Investigating the Effects of Annealing on the Mechanical Properties of FFF-Printed Thermoplastics, Journal of Manufacturing and Materials Processing 4(2) (2020).

[67] G.D. Goh, Y.L. Yap, S. Agarwala, W.Y. Yeong, Recent Progress in Additive Manufacturing of Fiber Reinforced Polymer Composite, Advanced Materials Technologies 4(1) (2019) 1800271.

[68] K.R. Hart, R.M. Dunn, J.M. Sietins, C.M.H. Mock, M.E. Mackay, E.D. Wetzel, Increased fracture toughness of additively manufactured amorphous thermoplastics via thermal annealing, Polymer 144 (2018) 192-204.

[69] S.A. Tronvoll, T. Welo, C.W. Elverum, The effects of voids on structural properties of fused deposition modelled parts: a probabilistic approach, International Journal of Advanced Manufacturing Technology 97(9-12) (2018) 3607-3618.

[70] H.J. Kitchen, S.K. Vallance, J.L. Kennedy, N. Tapia-Ruiz, L. Carassiti, A. Harrison, A.G. Whittaker, T.D. Drysdale, S.W. Kingman, D.H. Gregory, Modern Microwave Methods in Solid-State Inorganic Materials Chemistry: From Fundamentals to Manufacturing, Chemical Reviews 114(2) (2014) 1170-1206.

[71] C.L. Tucker, FLOW REGIMES FOR FIBER SUSPENSIONS IN NARROW GAPS, Journal of Non-Newtonian Fluid Mechanics 39(3) (1991) 239-268.

[72] L. Woo Il, G.S. Springer, Microwave Curing of Composites, Journal of Composite Materials 18(4) (1984) 387-409.

[73] Y.P. Ning, J.Y. Xu, H. Huang, Z.H. Wang, A. Yao, Effect of Carbon Fiber Admixture and Length on Microwave Deicing Efficiency of Airport Road Surface Concrete, Advances in Materials Science and Engineering 2022 (2022).

[74] H. Fan, C. Hartshorn, T. Buchheit, D. Tallant, R. Assink, R. Simpson, D.J. Kisse, D.J. Lacks, S. Torquato, C.J. Brinker, Modulus-density scaling behaviour and framework architecture of nanoporous self-assembled silicas, Nature Materials 6(6) (2007) 418-423.

[75] J.E. Seppala, S.H. Han, K.E. Hillgartner, C.S. Davis, K.B. Migler, Weld formation during material extrusion additive manufacturing, Soft Matter 13(38) (2017) 6761-6769.

[76] A. Nogales, E. Gutierrez-Fernandez, M.C. Garcia-Gutierrez, T.A. Ezquerra, E. Rebollar, I. Sics, M. Malfois, S. Gaidukovs, E. Gecis, K. Celms, G. Bakradze, Structure Development in Polymers during Fused Filament Fabrication (FFF): An in Situ Small- and Wide-Angle X-ray Scattering Study Using Synchrotron Radiation, Macromolecules 52(24) (2019) 9715-9723.

Appendix

A.1. Selection of microwave conditions

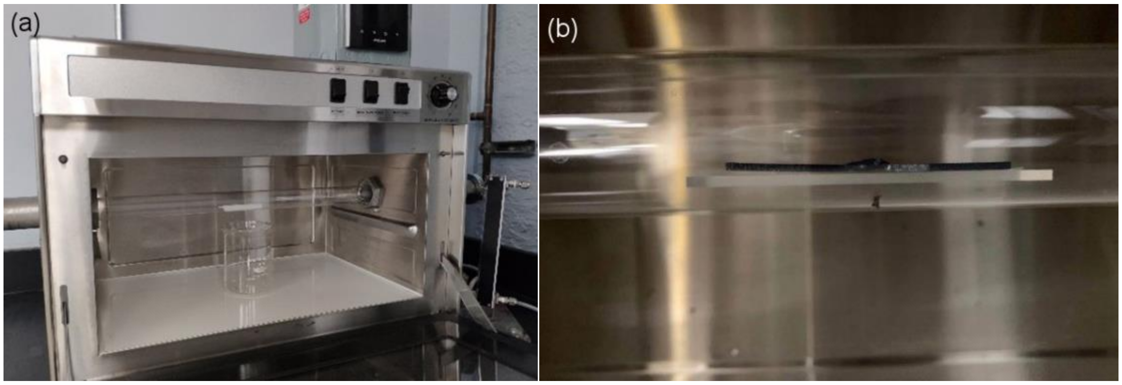

Figure S1. (a) The microwave oven used (BP-210, Microwave Research and Applications, Inc.). Quartz tube is placed through the chamber and connected with inert gas channel. (b) Photo of a tensile bar loaded within the quartz tube with the microwave door open.

Figure S2. (a) Carbon PEEK tensile bars under different microwave power and time combination. (b) Close look on 2100w 20sec specimen within ceramic container. Specimen melted and degraded after excessive energy input.

A.2. Tensile properties

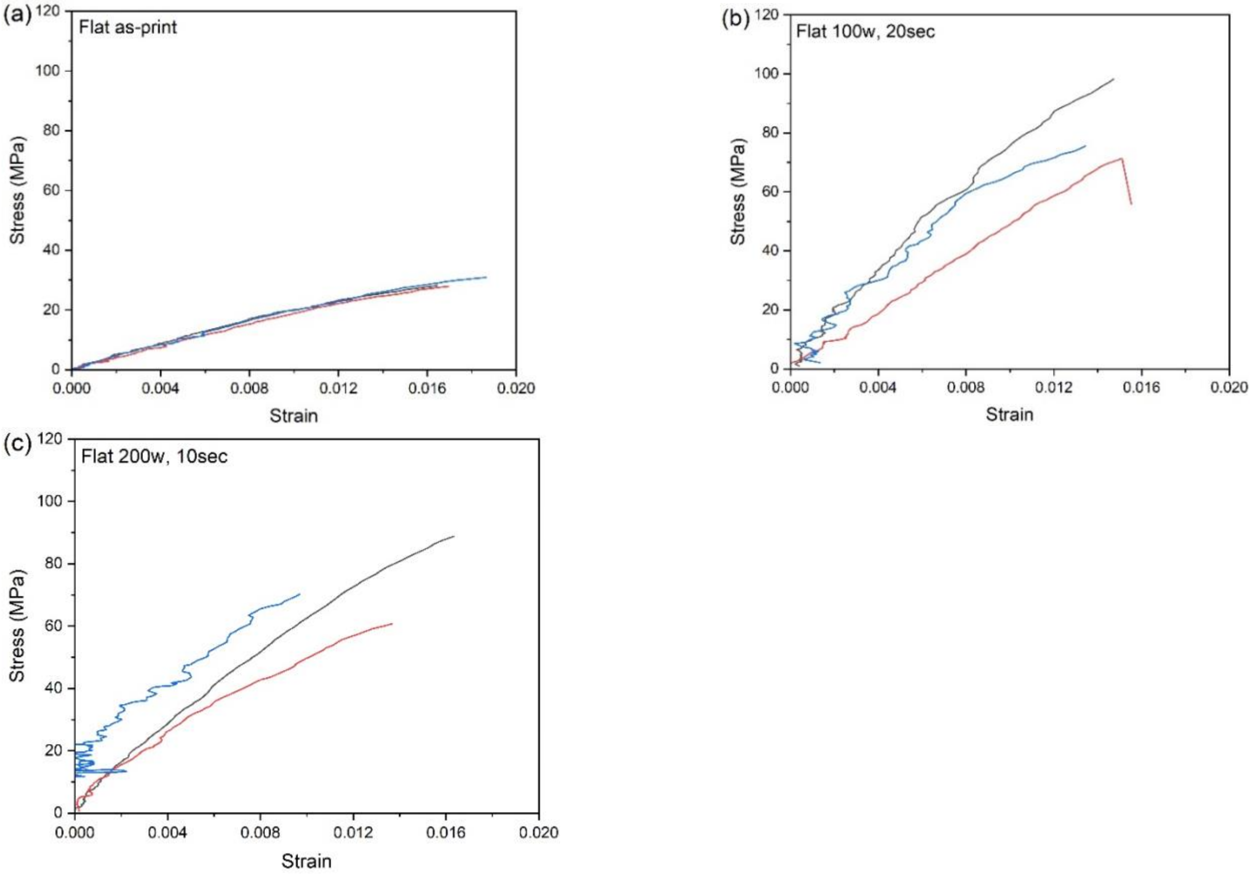

Figure S3. Stress-strain curves for all specimens printed in flat build orientation for (a) as-printed and microwave post-processing with (b) 100W for 20 s and (c) 200 W for 10 s. The different colors represent different specimens with nominally identical processing.

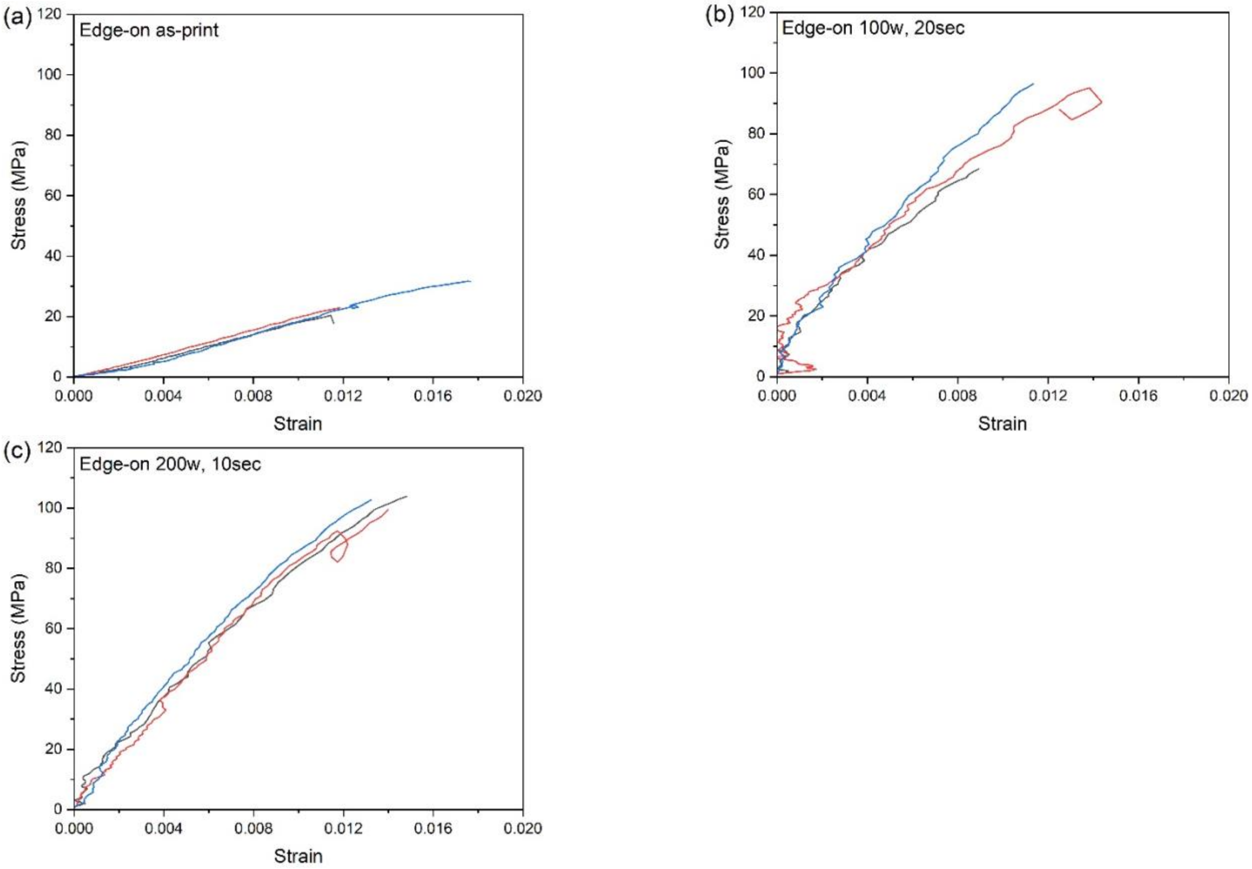

Figure S4. Stress-strain curves for all specimens printed in edge-on build orientation for (a) as-printed and microwave post-processing with (b) 100W for 20 s and (c) 200 W for 10 s. The different colors represent different specimens with nominally identical processing

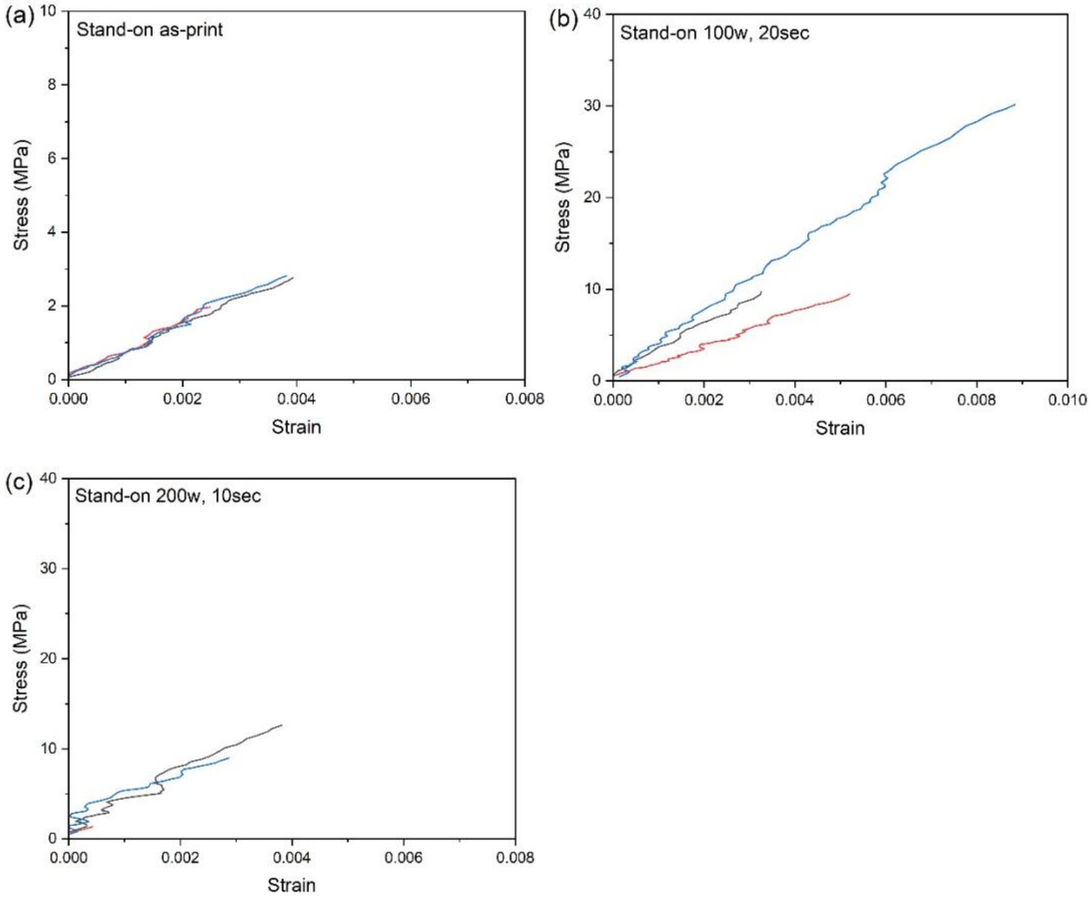

Figure S5. Stress-strain curves for all specimens printed in stand-on build orientation for (a) as-printed and microwave post-processing with (b) 100W for 20 s and (c) 200 W for 10 s. The different colors represent different specimens with nominally identical processing

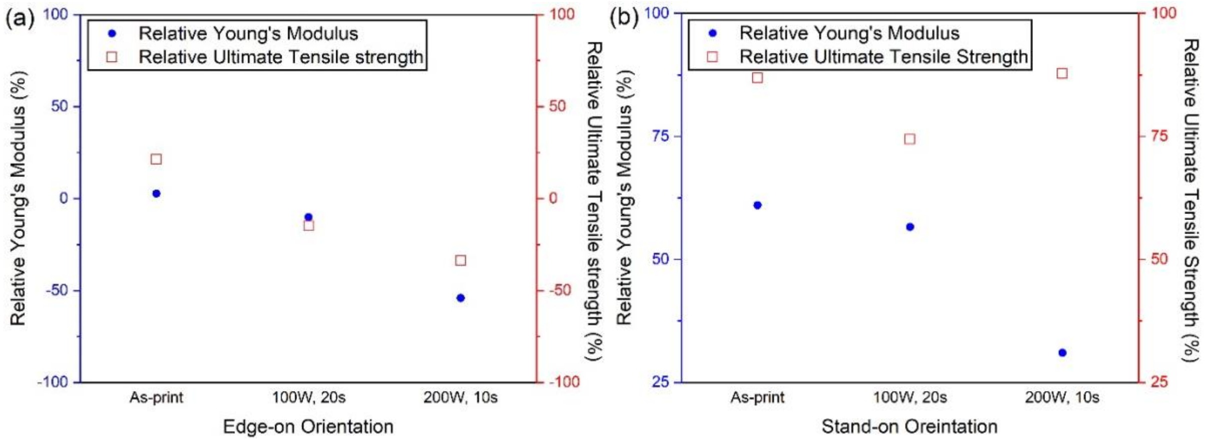

Figure S6. Degree of anisotropy of mechanical properties for additive manufactured carbon PEEK before and after microwave annealing (a) edge-on orientation (b) stand-on orientation.

$$\Delta(\%)_{YM} = \frac{YM_{flat} - YM_{edge-on,\ stand-on}}{YM_{flat}}$$

$$\Delta(\%)_{UTS} = \frac{UTS_{flat} - UTS_{edge-on,\ stand-on}}{UTS_{flat}}$$

Equations for calculating degree of anisotropy for Young's modulus and strain at break. Note that the value of mechanical properties of flat orientation at given post-processing conditions are used as reference for calculating degree of anisotropy for these conditions.

A.3. PEEK crystallinity

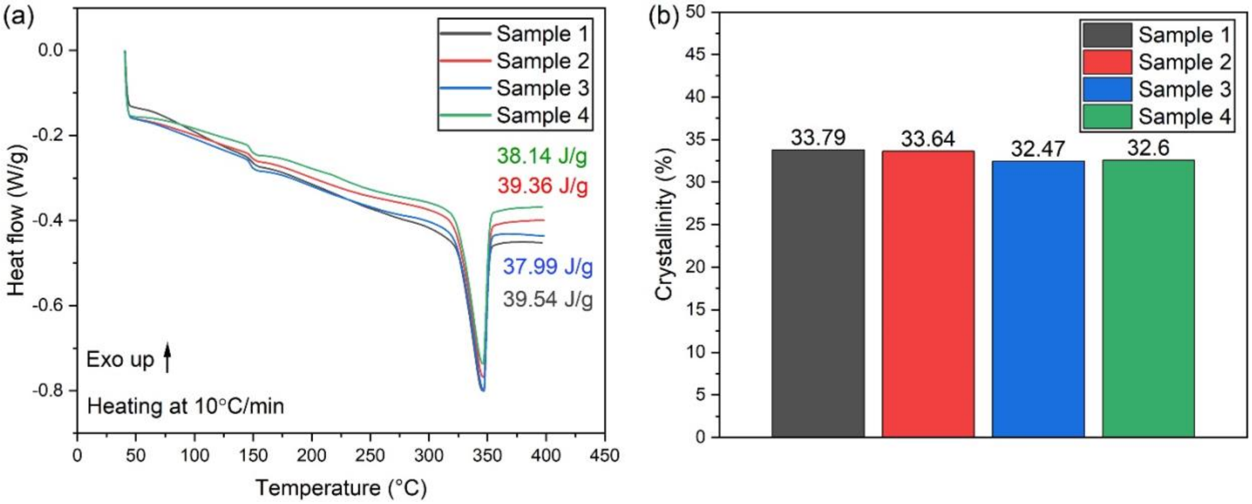

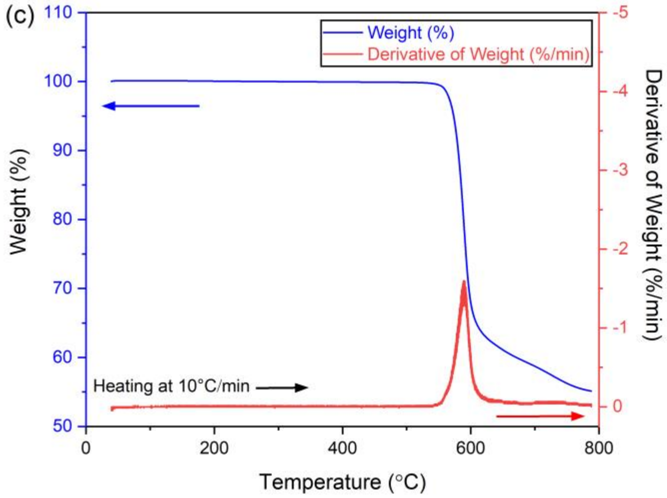

Figure S7. (a) 1st heating curve of cPEEK filament from different locations along the filament. (Note: the heat of fusion listed includes the mass of PEEK and carbon). (b) Crystallinity of PEEK for the corresponding filament segments. The crystallinity of the filament was 33.1 ± 0.7 %. The crystallinity is calculated considering remove 10wt% carbon fiber content within thermogram. (c) TGA decomposition analysis of cPEEK filament. The high char yield from PEEK prohibits direct determination of the carbon loading from TGA.

Table S1. XRD summary of flat orientation as-printed sample.

2θ	FWHM	d -Spacing (Å)	Scherrer particle size (Å)	Average crystal size (nm)
18.67	0.85	4.75	98.71	10.49
20.62	0.62	4.3	135.01	
22.59	0.85	3.93	99.42	
28.68	0.99	3.11	86.34	

Table S2. XRD summary of flat orientation sample after 100 W, 20 s microwaves

2θ	FWHM	d-Spacing (Å)	Scherrer particle size (Å)	Average crystal size (nm)
18.69	1.05	4.74	80.06	8.40
20.64	1.37	4.23	61.65	
22.66	1.17	3.92	72.36	
28.74	0.70	3.10	122.12	

Table S3. XRD summary of flat orientation sample after 200 W, 10 s microwaves.

2θ	FWHM	d-Spacing (Å)	Scherrer particle size (Å)	Average crystal size (nm)
18.70	0.97	4.74	86.49	
20.68	1.27	4.29	66.41	8.94
22.70	0.99	3.91	85.08	
28.81	0.72	3.09	119.62	

Table S4. XRD summary of edge-on orientation as-printed sample.

2θ	FWHM	d-Spacing (Å)	Scherrer particle size (Å)	Average crystal size (nm)
18.69	1.41	4.74	59.64	
20.67	1.27	4.29	66.27	7.60
22.56	1.25	3.94	67.61	
28.79	0.77	3.10	110.66	

Table S5. XRD summary of edge-on orientation sample after 100 W, 20 s microwaves.

2θ	FWHM	d-Spacing (Å)	Scherrer particle size (Å)	Average crystal size (nm)
18.62	1.22	4.76	68.82	
20.60	1.21	4.31	69.50	7.70
22.57	1.27	3.93	66.36	
28.71	0.83	3.11	103.23	

Table S6. XRD summary of edge-on orientation sample after 200 W, 10 s microwaves

2θ	FWHM	d-Spacing (Å)	Scherrer particle size (Å)	Average crystal size (nm)
18.71	1.13	4.74	74.37	
20.70	1.30	4.28	65.05	7.59
22.71	1.25	3.91	67.72	
28.82	0.89	3.09	96.42	

Table S7. XRD summary of stand-on orientation as-printed sample.

2θ	FWHM	d-Spacing (Å)	Scherrer particle size (Å)	Average crystal size (nm)
18.66	1.14	4.75	73.64	7.43
20.58	1.35	4.31	62.60	
22.54	1.35	3.94	62.64	
28.67	0.87	3.11	98.51	

Table S8. XRD summary of stand-on orientation sample after 100 W, 20 s microwaves.

2θ	FWHM	d-Spacing (Å)	Scherrer particle size (Å)	Average crystal size (nm)
18.55	1.97	4.78	42.59	6.37
20.38	1.04	4.35	81.10	
22.23	2.02	3.99	41.77	
28.52	0.96	3.13	89.45	

Table S9. XRD summary of stand-on orientation sample after 200 W, 10 s microwaves.

2θ	FWHM	Spacing d (Å)	Scherrer particle size (Å)	Average crystalline size (nm)
18.56	1.40	4.78	59.98	7.46
19.94	0.79	4.45	106.77	
21.99	2.83	4.04	29.91	
28.52	0.84	3.13	101.65	

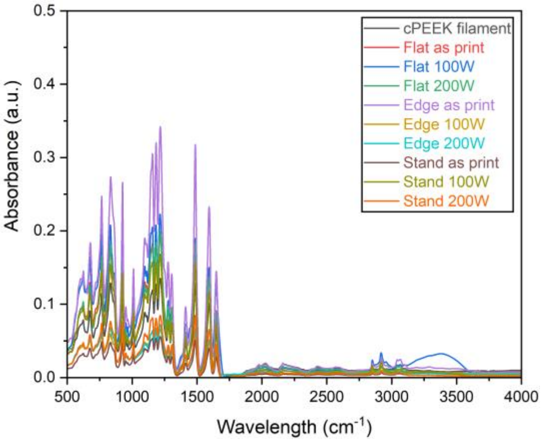

Figure S8. FTIR spectra within gauge region of the tensile specimens for a variety of build orientations and microwave post processing conditions. There are limited differences in the spectra except in the case of the Flat specimen with 100 W microwave post processing where there is the immergence of a broad peak between 3000-3500 cm-1, which is likely associated with formation of hydroxyl moieties.

A.4. Micro Voids and Carbon Fiber Orientation

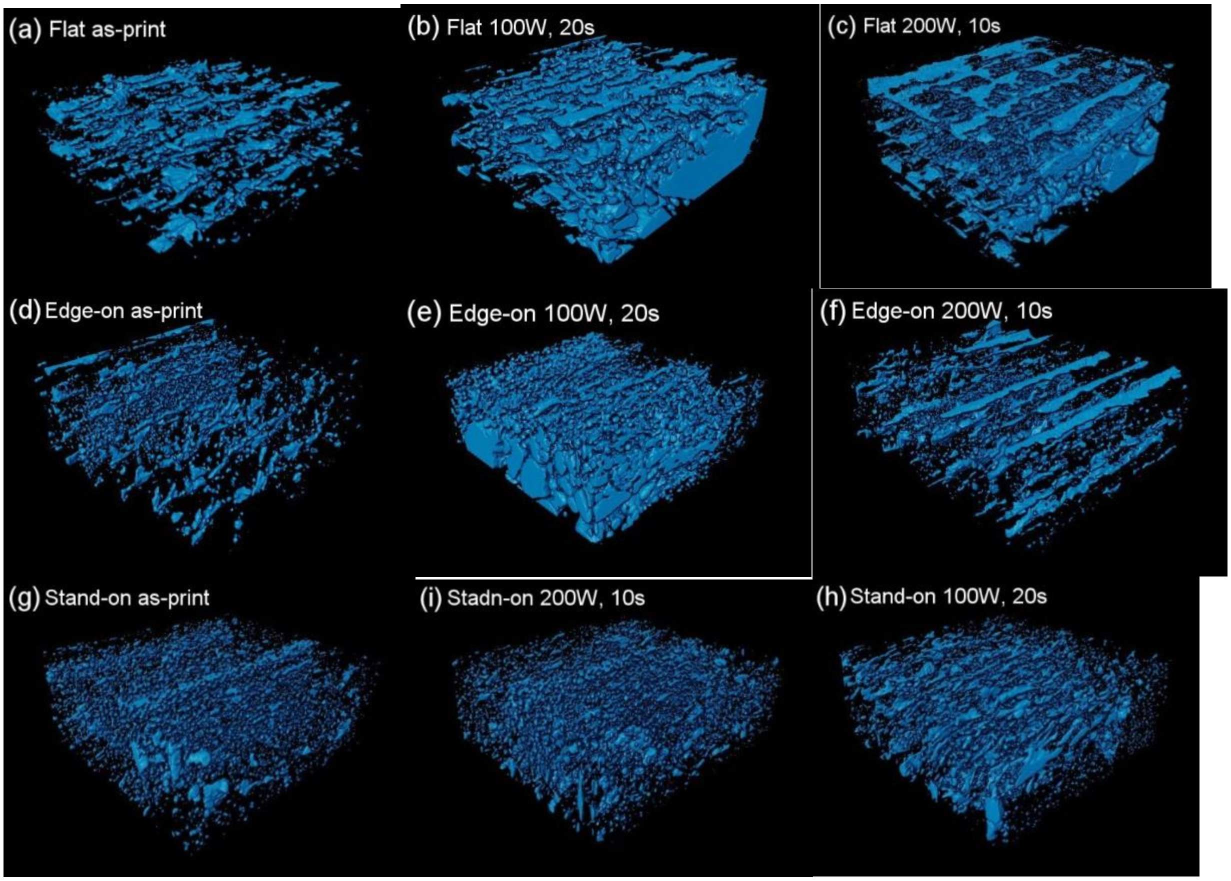

Figure S9. µCT reconstruction of voids based on size and locations within define volume. (a) flat as-print (b) flat 100W, 20s (c) flat 200W, 10s (d) edge-on as-print (e) edge-on 100W, 20s (f) edge-on 200W, 10s (g) stand-on(h) stand-on 100W, 20s and (i) stand-on 200W, 10s

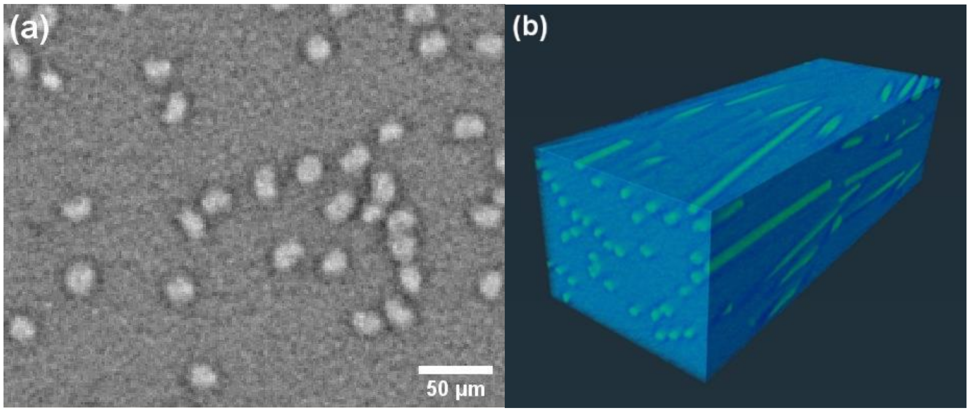

Figure S10. µCT analysis on single printing line alone the print direction. (a) the cross-section of print line. (b) Reconstruction volume of the ROI for calculating fiber volume fraction percentage and Herman's factor. The calculation of carbon fiber weight fraction percentage assumed the carbon fiber density is 1.79 g/cm^3 and PEEK density is 1.32 g/cm^3 with volume fraction percentage measured by µCT of 7.96% and 92.04%, respectively.